THE UNIVERSITY OF MICHIGAN
COLLEGE OF ENGINEERING

Department of Aerospace Engineering

Gas Dynamics Laboratories

Technical Report

WALL PRESSURE FLUCTUATIONS BENEATH AN AXIALLY SYMMETRIC TURBULENT BOUNDARY LAYER ON A CYLINDER

Chi-Sheng Yang

William W. Willmarth

ORA Project 02149

under contract with

DEPARTMENT OF THE NAVY
OFFICE OF NAVAL RESEARCH
CONTRACT NO. N00014-67-A-0181-0015
WASHINGTON, D. C.

administered through

OFFICE OF RESEARCH ADMINISTRATION
ANN ARBOR

August 1969

ABSTRACT

Measurements of the turbulent pressure field on the outer surface of a three inch diameter cylinder aligned with the flow were made at a point approximately 24 feet downstream of the origin of the turbulent boundary layer in an air stream of 145 ft/sec. The boundary layer thickness was 2. 78 inches and the Reynolds number based on momentum thickness was 2.62×10^4.

The wall-pressure measurements were made with pressure transducers constructed from 0. 06 inch diameter lead-zinconate-titnate disks mounted flush with the wall. The measurements included root-mean-square, power spectrum and correlations of the wall pressure and were compared with the existing experimental results for the turbulent wall pressure filed beneath a plane boundary layer.

The root-mean-square wall pressure was 2. 42 times the wall shear stress, somewhat lower than that measured beneath a plane boundary layer. The general shape of the normalized power spectrum was similar to the spectrum associated with a plane boundary layer. However, at high frequencies ($\omega\delta^*/U_\infty > 10$) the spectrum contains approximately twice the energy density measured in the plane boundary layer.

The streamwise convection speed deduced from longitudinal space-time correlation measurements was almost identical to that obtained in the plane boundary layer. The rate of decay of the maxima of the space-

time correlation of the pressure produced by the convected eddies was twice as fast as in a plane boundary layer. The longitudinal and transverse scale of the pressure correlation were approximately equal, in a plane boundary layer the transverse scale is larger than longitudinal scale, and were one-half or less than the longitudinal scale in the plane boundary layer. It is concluded that the effect of the transverse curvature of the wall is an overall reduction in size of pressure-producing eddies. The reduction in transverse scale of the larger eddies is greater than that of the smaller eddies. The smaller eddies then decay more rapidly and produce greater spectral densities at high frequencies owing to the unchanged convection speed.

TABLE OF CONTENTS

LIST OF ILLUSTRATIONS

NOMENCLATURE

a	radius of circular cylinder
$E(k_1, k_3, \omega)$	spectrum of the wall pressure
f	frequency
k_1, k_3	wave number
P	mean pressure
p	fluctuating wall pressure
q_∞	free stream dynamic pressure
$Q_{pp}(x_1, x_3, \tau)$	double pressure correlation
$Q'_{pp}(x_1, x_3, \tau, \omega)$	double pressure correlation in a narrow frequency band which has central frequency at ω
R	radius of the pressure transducer
R_a	Reynolds number $U_\infty a/\nu$
R_θ	Reynolds number $U_\infty \theta/\nu$
R_{δ^*}	Reynolds number $U_\infty \delta^*/\nu$
$R_{pp}(x_1, x_3, \tau)$	correlation coefficient of wall pressure
$R'_{pp}(x_1, x_3, \tau, \omega)$	correlation coefficient of wall pressure in a narrow frequency band which has central frequency at ω
$r = y + a$	radius distance from axis of the cylinder
U	mean velocity in the boundary layer in the stream direction
U_∞	free-stream velocity
U_τ	wall friction velocity
U_c	convection speed of the pressure-producing turbulent eddies
u	fluctuating velocity in x direction
V	mean velocity in the boundary layer in y direction
v	fluctuating velocity in y direction

x	distance parallel to wall, increasing in the stream direction
y	distance normal to wall, increasing away from wall
z	distance parallel to wall and perpendicular to stream direction, forming a right-hand Cartesian coordinate system with x and y
x_1, x_2, x_3	spatial separation of pressure transducers in x, z directions
Γ	temporal cross-spectral density of the wall pressure
δ	boundary layer thickness
δ^*	boundary layer displacement thickness
θ	boundary layer momentum thickness
Λ_1	integral scale of R_{pp} in x_1 direction
Λ_3	integral scale of R_{pp} in x_3 direction
Λ_τ	integral time scale of R_{pp}
ν	kinematic viscosity
ρ	density
τ	time delay
τ_c	convection time of pressure-producing turbulent eddies
τ_w	wall shear stress
Φ	meridian angle
$\phi(\omega)$	power spectrum
Ψ	stream function
ω	circular frequency
$\bar{(\ )}$	time average

I. INTRODUCTION

Knowledge of the pressure fluctuations beneath turbulent boundary layers is desired for numerous problems in fluid mechanics. The problems include: aerodynamic sound produced by turbulence in the boundary layer when the surface is rigid, vibration and sound radiation produced when the turbulent boundary layer is developed on a slightly flexible surface that is set in motion by the pressure fluctuations, and the new knowledge of turbulence structure in a boundary layer that can be obtained from wall pressure measurements

Most of our knowledge of wall pressure fluctuations has been obtained from experimental measurements beneath the flat plate boundary layer. There are a great many papers reporting measurements of wall pressure fluctuations on a flat plate for various conditions (which include subsonic and supersonic free stream velocities with various free stream pressure gradients and for boundary layers developed on smooth and rough surfaces).

At low subsonic speeds with zero free stream pressure gradient, the investigations of Bull (1963), Willmarth (1958a) and Willmarth and Woolridge (1962) are representative of the results of pressure measurements beneath flat plate boundary layers developed on smooth walls at high Reynolds numbers. In general, it has been observed that the wall pressure fluctuations are random without periodic components and have

power spectra roughly similar in shape to the spectrum of the turbulent velocity component normal to the wall. Using the method of space-time correlation measurements, it was discovered, Willmarth (1958a), that the pressure fluctuations were convected with a speed of approximately 0.8 U_∞. More detailed investigations, Willmarth and Woolridge (1962) and Bull (1963) have shown that the convection velocity varies with streamwise spatial separation of the measuring stations and that for small spatial separation the convection velocity is low, 0.56 U_∞. The increase in convection velocity with streamwise separation of measuring points is attributed to the more rapid decay of the smaller pressure producing eddies which on the average lie closer to the wall and are moving slower than those eddies which are larger and, therefore, move at higher speeds owing to the higher speed at a greater distance from the wall.

The purpose of the present investigation of the pressure fluctuations beneath the boundary layer on the outside of a cylinder whose axis is aligned with the free stream is to determine the effect of transverse curvature on the wall pressure fluctuations. Ideally, the determination of transverse curvature effects should be made by comparing measurements made on a cylinder and on a flat plate with exactly the same Reynolds number, pressure gradient, Mach number and surface roughness. Measurements have been made in the boundary layer on a smooth flat

plate, Willmarth and Wooldridge (1962), at slightly higher Reynolds numbers, based on momentum thickness, $R_\theta = 38,000$, than could be obtained on the cylinder, $R_\theta = 26,200$. We also will compare measurements on the cylinder with the measurements of Bull (1963), obtained beneath a flat plate boundary layer at Reynolds number, $R_\theta = 19,500$.

Our knowledge of turbulent boundary layers with transverse curvature is not as extensive as it is for the flat plate boundary layer and is restricted to measurements and similarity laws for mean quantities only. The work of Richmond (1957), Yu (1958), Yasuhara (1959), Reid and Wilson (1963), and Rao (1967) contain measurements and in some cases similarity laws for mean properties of turbulent boundary layers with varying amounts of transverse curvature.

It is often profitable in attempting to understand mean properties of the flow in a turbulent boundary layer to first consider the flow in a laminar boundary layer. It has been found by Glauert and Lighthill (1955) that the laminar boundary layer developed on a cylinder (when transverse curvature effects are large) has a much fuller profile than the Blasius boundary layer on a flat plate. In fact, the velocity near the wall is proportional to the logarithm of the distance from the cylinder axis and departs from that of the Blasius profile (in which u is linearly proportional to y near the wall) as the cylinder radius is reduced. The cause of this behavior (as was clearly explained by Glauert and Lighthill

(1955)) is that "the shearing force, on a cylinder of unit length, is equal to the shear stress μ du/dy multiplied by the circumference 2π (a + y) of the cylinder, and this force must be independent of y in the region where the acceleration of the fluid is negligible, that is, near the solid boundary."

One can expect that the presence of turbulence in a boundary layer with transverse curvature will increase the rate of momentum exchange (just as it does in a flat plate boundary layer) with the result that the velocity profile will be fuller, the skin friction increased, and the streamwise rate of growth of the boundary layer thickness decreased.

The effect of transverse curvature on the structure of turbulence in the boundary layer and on the pressure fluctuations beneath it have not been studied. As a result of the present wall pressure measurements, we have been able to qualitatively explain some of the effects of transverse curvature on turbulence structure.

II. WIND TUNNEL AND CYLINDRICAL MODEL

A. WIND TUNNEL FACILITY

The experiments were carried out in the test section of the 5 x 7 foot low speed wind tunnel at the Gas Dynamics Laboratories, Department of Aerospace Engineering, The University of Michigan. The wind tunnel test section is 25 feet long and is indoors. The settling chamber, fan and steel ducting that recirculates the air are out of doors. The total distance around the wind tunnel circuit is 332 feet and the contraction ratio of the nozzle is 15:1.

The sound field in the tunnel test section has been measured by Willmarth and Woolridge (1962). They stated: "The sound field in the test section was first measured with a pressure transducer located on the stagnation line of an airfoil-shaped body exposed to the free stream. The spectrum of the stagnation pressure fluctuations had peaks at 135 and 200 Hz. The wall pressure correlation measurements on the floor of the test section which were made later showed a small peak at negative time delay which was caused by sound propagating upstream. From the measurements, it was finally determined that the sound energy amounted to approximately 1/20 of the energy in the turbulent wall pressure fluctuations." In the present wall pressure correlation measurements the sound energy is approximately 1/50 of the energy in turbulent wall pressure

fluctuations. The reduction of sound level was accomplished by better sealing against air leaks at the diffuser entrance and by reducing structural vibration in the downstream region of the test section and diffuser entrance.

The free-stream turbulence level measured by Tu and Willmarth (1966) at 200 ft/sec free stream speed was $\sqrt{\overline{u}^2}/U_\infty = 2.50 \times 10^{-3}$ in the flow direction. The configuration of the wind tunnel has not been changed since that time.

B. CYLINDRICAL MODEL

A 40 foot long, 3 inch diameter cylindrical model on which the boundary layer measurements were made was installed along the centerline of the wind tunnel. It consisted of a 2 inch steel tubing used as the backbone of the model and a 3 inch steel tubing used as the aerodynamic surface. The 3 inch tubing was located on the inner 2 inch tubing by means of adjustable set-screws. A 6 inch long ellipsoid of revolution and an 8 inch cone, both made of wood, were attached to the upstream and downstream end of the model respectively. The supports for the 2 inch tubing were so designed that they could furnish moments to reduce the mid-span deflection of the tubing (Fig. 1). Upstream support consisted of 5 streamlined aircraft wires. Two wires, T_2, and one wire, T_1, produced a counter-clock-wise moment. The other two wires at the bottom were dummy wires. The downstream support was a unistrut frame with two

unequal height columns (Fig. 2). When the 2 inch tubing was bolted on the columns, a clock-wise moment was produced. The deflection of the model in the test section of the tunnel was reduced to a minimum value by properly adjusting the forces T_1 and F_2.

The wind velocity near the wire, T_1, was low, approximately $0.09\ U_\infty$, therefore, the larger deflection at the front end of the model did not effect the symmetry of the boundary layer flow in the test section. The wind velocity near the wires, T_2, was approximately $0.15\ U_\infty$. Since the terminals of the wires near the surface of the model were 1/4 inch in diameter, they caused an asymmetry of the flow field around the cylinder in the test section. Four airfoil shaped filets, made from balsa wood, were used to reduce the wake from the junction of the support wires and cylindrical surface with satisfactory results as described below.

A circumferential pitot tube array (Fig. 4, left), which consisted of 8 tubes 0.65 inch above the surface of the model, was used to measure the circumferential velocity distribution at 16 feet and 24 feet from the entrance of the test section. Initially the velocity distribution was very asymmetric with low velocity regions at four circumferential positions in the wake of the four upstream support wires. The use of balsa wood filets (see above) reduced the wake from the upstream wire supports and careful alignment of the model by moving the downstream supporting

struts reduced the asymmetry of the boundary layer to an acceptable level. The circumferential velocity distribution measured at the pressure transducer station (x = 24 ft) for three different free stream velocities are plotted on Fig. 3. The largest velocity deviation was 0.02 U_∞.

At its final position, the maximum vertical deflection of the model in the test section of the tunnel was 0.39 inches, the corresponding slope was 0.2% approximately. The maximum lateral deflection was 0.25 inches, the corresponding slope was 0.1% approximately.

III. INSTRUMENTS AND EXPERIMENTAL METHODS

A. INSTRUMENTS AND METHODS FOR MEASURING MEAN PROPERTIES OF THE FLOW

To measure the velocity profile very near the surface of the cylinder a pitot tube was installed on a traversing device (Fig. 4, right). The pitot tube was a 0.042 inch diameter stainless hypodermic tubing with a flattened mouth. The dimensions of the mouth of the tube are shown in Fig. 5. It was used in the Reynolds number range $50 < R = hU/\nu < 250$ where h was the internal height of the mouth. The correction to the reading of the tube owing to viscous effects was negligible (see McMillan (1954)). The maximum angle of attack of the pitot tube was 10 degrees. It was experimentally confirmed that the angle of attack did not affect the total pressure reading up to an angle of 15 degrees (see Alexander (1953)). The pitot tube was moved normal to the surface by the operator outside the test section, using a linkage and worm gear mechanism that was driven by a flexible shaft. The distance of the pitot tube from the surface was measured with a cathetometer focused on the pitot tube through the window of the tunnel.

The static pressure was measured with a static tube in contact with the surface of the cylinder. This static tube was a long 0.065 inch diameter hypodermic tubing with one end sealed. A 0.035 inch diameter hole was drilled in the tube 3 1/2 inches from the sealed end.

The difference between pitot and static pressure was measured with a precision single-tube manometer* with a resolution of .001 inch using water as the indicating liquid.

The velocity profiles quite far from the wall, $y/\delta > 0.2$, were measured with a pitot tube rake which consisted of 10 pitot tubes and 2 static tubes at different heighths from the wall (Fig. 4, middle).

The wall shear stress was measured according to Preston's method (Preston (1954)) using a 0.042 inch diameter pitot tube in contact with the surface of the cylinder. The calibration given by Smith and Walker (1958) was used for calculation of wall shear stress.

B. INSTRUMENTS AND METHODS FOR MEASURING TURBULENT PRESSURE FIELD

1. Pressure Transducers

At the test station, the lower half of the model was replaced by a 4 1/2 inch long, 3 inch O.D. semi-cylindrical lead shell (Fig. 6). There were 13 transducer elements, which were 0.06 inch diameter and 0.020 inch thick lead-zinconate-titnate (PZT-5) disks mounted permanently flush with the outer surface of the lead shell. The arrangement of the transducers which was selected to efficiently obtain the spatial correlation of the pressure field is shown on Fig. 7.

---

* The Meriam Instrument Co., Micro-Manometer Model 34 FB2

Fig. 8-a shows the cross section of a single transducer plug mounted in the lead shell. A fine copper wire (0. 002 inch diameter) was attached to the front surface of the phenolic plug and brought out through the hole in it which was then filled with wax. The PZT-5 disk was glued on the plug with conducting cement. * This plug was then inserted into a 0. 063 inch diameter hole drilled through the lead shell. The position of the plug was so adjusted that the PZT-5 disk was flush with the lead surface. Having put the plug in position, the remainder of the hole was filled with vacuum sealing wax, a product of Central Scientific Company. On the front surface, the transducer was electrically connected to the lead shell with a thin coat of conducting silver paint. *

The cross section of the triple transducer plug is shown on Fig. 8-b. The construction differed from the single transducer plug in that an additional brass sleeve was used and the method of ground connection was altered. The outer surface of the brass sleeve was curved to match the surface curvature of the lead shell. The electrical connection between the brass and the PZT-5 disks was provided by gluing a piece of aluminized mylar plastic sheet (0. 0005 inches thick) on the surface. The brass sleeve was in contact with lead.

---

*SC 12 MicroCircuits Co., New Buffalo, Michigan.

Thirteen short Microdot coaxial cables with Microdot connectors at one end were glued on the inner surface of the lead shell with epoxy cement. * The copper wires at the back of the transducer plugs were soldered to the central conductor of the cables. Two seven foot long Microdot coaxial cables with additional outer shielding to make a tri-axial cable were used to conduct the transducer signals to the input of the cathode followers and preamplifiers. To reduce parasitic capacitance of the long cable, the coaxial cable shield was driven by a voltage proportional to the transducer signal and the additional outer shield outside the cable was used as ground (Fig. 9).

In order to seal the air gap between the lead shell and the steel tubing, the lead shell was held on the model by a thin rubber cuff (0.008 inch thick). Four rubber O-rings were placed between the contact surfaces of the lead and the steel to prevent the transmission of vibration of the tunnel structure and the model to the lead shell and transducers.

The capacitance of the pressure transducer was 32 pf. The use of a driven shield, see Fig. 9, effectively reduced the capacity of the long cables leading to the preamplifiers and cathode followers to a low value. The frequency response of the transducers was assumed to be flat over the frequency range of interest, $f \leq 50,000$ Hz. Willmarth (1958b) has shown

---

*Epo-lux Steelcote Mfg. Co., No. 185A.

by shock tube calibration that larger transducers than the present transducers which were made in a similar manner did have a flat frequency response up to at least 50,000 Kz. The absolute calibration of the pressure transducers was carried out "in situ" with the lead shell installed on the cylindrical model. A previously calibrated transducer, * Willmarth and Wooldridge (1962), and the new pressure transducers were put inside a Helmholtz resonator which was made from a bottle whose bottom was cut to fit the cylinder. The joint was sealed with clay and the Helmholtz resonator was excited at 250 Hz by a carefully placed low speed air jet. The calibration was obtained by comparing the output of the two transducers inside the Helmholtz resonator. The sensitivity of the transducers was typically 1.32×10^{-6} volts/dyne/cm^2.

2. Electronic Equipment

The transducers were connected to a cathode follower with high input impedence of 1.2×10^{8} ohms (Fig. 9) followed by a low noise preamplifier and amplifier system with a maximum gain of 10^5, see Willmarth and Wooldridge (1962). The band width of the amplifier was adjustable between 1 Hz and 160 KHz. The electrical signals from the pressure transducers were recorded on a three channel Ampex FR 1100 tape recorder which had a band width from DC to 20 KHz. The root-mean-square wall pressure was measured with a Ballantine model 320 true RMS meter.

---

*We checked the 1962 calibration using the 1962 method (an enclosed volume variable over a small range with a piston) and found no appreciable change in the calibration over 6 years!

The spectrum of the fluctuating wall pressure was obtained by passing the signal through a Tektronix Type 115 spectrum analyzer plug-in unit which was driven by a Tektronix Type 544 oscilloscope. The output was recorded on a Hewlett Packard Model 2DR-2M x-y recorder.

The correlations of the wall pressure were measured with a Princeton Applied Research Model 101 correlation function computer whose output was recorded with the above x-y recorder. Two Kron-Hite Model 310-AB variable band pass filters were used for correlation measurements in narrow frequency bands.

IV. MEAN FLOW FIELD

A. EQUATIONS OF MOTION

The momentum equations for axially symmetric mean motion in a turbulent flow written in cylindrical coordinates are

$$U\frac{\partial U}{\partial x} + V\frac{\partial U}{\partial r} = -\frac{1}{\rho}\frac{\partial P}{\partial x} + \nu\frac{1}{r}\frac{\partial}{\partial r}\left(r\frac{\partial U}{\partial r}\right) + \frac{\partial^2 U}{\partial x^2} - \frac{\partial \overline{U^2}}{\partial x} - \frac{1}{r}\frac{1}{\partial r}\left(r\,\overline{uv}\right) \tag{1}$$

and

$$U\frac{\partial V}{\partial x} + V\frac{\partial V}{\partial r} = -\frac{1}{\rho}\frac{\partial P}{\partial r} + \nu\frac{1}{r}\frac{\partial}{\partial r}\left(r\frac{\partial V}{\partial r}\right) + \frac{\partial^2 V}{\partial r^2} - \frac{1}{r}\frac{\partial}{\partial r}\left(\overline{rv^2}\right) - \frac{\partial}{\partial x}\overline{uv} \tag{2}$$

where U, V and P are mean quantities and it has been assumed that the free stream is parallel to the x axis and the velocity V is the radial velocity normal to the x axis.

Using the usual boundary layer approximations, the boundary layer equations are

$$U\frac{\partial U}{\partial x} + V\frac{\partial U}{\partial r} = -\frac{1}{\rho}\frac{\partial P}{\partial x} + \frac{\nu}{r}\left(r\frac{\partial U}{\partial r}\right) - \frac{1}{r}\frac{\partial}{\partial r}\left(r\,\overline{uv}\right) \tag{3}$$

and

$$\frac{\partial P}{\partial r} = 0 \tag{4}$$

with continuity equation

$$\frac{\partial U}{\partial x} + \frac{1}{r}\frac{\partial (rV)}{\partial r} = 0 \tag{5}$$

The corresponding boundary layer conditions are:

$$U = V = 0, \quad \overline{uv} = 0 \qquad \text{at} \qquad r = a$$

$$U = U_\infty, \quad V = 0, \quad \overline{uv} = 0 \qquad \text{at} \qquad r = a + \delta$$

where a is the body radius and δ is the boundary layer thickness.

With the aid of continuity equation and the fact that $dp/dx = - \rho U_\infty \, dU_\infty/dx$, Eq. (3) can be integrated with respect to r from r = a to r = a + δ. Hence, the momentum integral equation for axially symmetric turbulent boundary layer is obtained:

$$2a \frac{\tau_w}{\rho} = \frac{d}{dx} \left\{ U_\infty^2 \left[(\theta + a)^2 \right] \right\} + U_\infty \left[(\delta^* + a)^2 \right] \frac{dU_\infty}{dx} \tag{6}$$

where τ_w is the wall friction. The displacement thickness (δ^*) and the momentum thickness (θ) for a fluid of constant density are defined by

$$(\delta^* + a)^2 - a^2 = \int_{a^2}^{(\delta+a)^2} \left(1 - \frac{U}{U_\infty} \right) dr^2 \tag{7}$$

and

$$(\theta + a)^2 - a^2 = \int_{a^2}^{(\delta+a)^2} \left(1 - \frac{U}{U_\infty} \right) \frac{U}{U_\infty} \, dr^2 \tag{8}$$

for U_∞ = Constant, Eq. (6) becomes

$$\frac{\tau_w}{\rho} = U_\infty^2 \left(1 + \frac{\theta}{a} \right) \frac{d\theta}{dx} \tag{9}$$

Hence the skin friction coefficient is

$$C_f \frac{\tau_w}{\frac{1}{2}\rho U_\infty^2} = 2\left(1 + \frac{\theta}{a}\right) \frac{d\theta}{dx} \tag{10}$$

B. SIMILARITY LAWS

The correct similarity laws for the mean flow in an axially symmetric boundary layer with zero pressure gradient have not yet been firmly established. If the amount of transverse curvature is not too large, the most logical approach might be to assume that the usual law of the wall and law of the wake are still valid. However, one must recognize immediately that there is an additional dimensional length parameter, the radius of curvature of the wall, a, in the problem. Thus, in the wall region dimensional considerations indicate a functional relationship

$$\frac{U}{U_\tau} = F\left(\frac{yU_\tau}{\nu} , \frac{aU_\tau}{\nu}\right) \tag{11}$$

and in the wake region,

$$\frac{U_\infty - U}{U_\tau} = G\left(\frac{y}{\delta} , \frac{\delta}{a}\right) \tag{12}$$

Here, we have made all the usual assumptions about the mean flow in the wall and wake region (see Clauser (1956)) and have simply added the additional length, a, the transverse radius of curvature of the wall.

It is quite possible that the traditional division of mean flow properties into a wall region and wake region may not be valid when the transverse curvature is large, $\delta/a \gg 1$. One may visualize a very small radius of curvature of the wall in which the region occupied by fluid motions obeying the law of the wall (which is assumed to be of the form of Eq. (11)) is a very small fraction of the region occupied by the turbulent boundary layer flow. In other words, the boundary layer on a slender rod ($a/\delta \to 0$) is almost all a wake-like flow and the region near the wall (which, if it is called the wall region, must be independent of free stream conditions) would be a very small region containing the viscous sublayer. It is possible that in the limit $a \to 0$ the wall region contains only the viscous sublayer.

In our present work we have been restricted to boundary layers in which $\delta/a \approx 2$. For this case we will assume that the traditional (but modified, see Eq. (11) and (12)) division of the mean flow into a wall region and a wake region is valid. In addition we will also adopt the procedure of Richmond (1957), for the flow in the region near the wall. Essentially what Richmond (1957) did (under Coles' guidance) was to assume that there was a region near the wall where the mean flow was dominated by the wall. He then obtained a law of the wall for the axisymmetric boundary layer using Coles' streamline hypothesis in that region. Coles' streamline hypothesis, Coles (1955), (which is true in the region near the wall of a two - dimensional turbulent boundary

layer) asserts that U/U_τ is constant on mean streamlines. Therefore, we can expect Richmond's procedure for the wall region of the axisymmetric boundary layer to be valid in the region near the wall where the turbulent flow is still essentially two-dimensional (or, in other words, when the ratio y/a is small). If y/a is not small, the similarity law obtained from the streamline hypothesis may be incorrect.

We will give for reference (since Richmond's paper is not readily available) a brief description of his procedure for obtaining the similarity law. He assumes (the streamline hypothesis) that U/U_τ is constant on the mean streamlines. Therefore, using the stream function, Ψ,

$$\frac{U}{U_\tau} = \phi\,(C\Psi) \tag{13}$$

or inverting the expression

$$\Psi = \frac{1}{C}\,H\left(\frac{U}{U_\tau}\right) \tag{14}$$

The continuity equation is

$$\frac{\partial U}{\partial x} + \frac{1}{r}\frac{\partial rV}{\partial r} = 0 \tag{15}$$

and defines the stream function

$$Ur = \frac{\partial \Psi}{\partial x} \quad ; \quad Vr = -\frac{\partial \Psi}{\partial x} \tag{16}$$

Thus, from Eq. (14)

$$U = \frac{1}{r}\frac{\partial \Psi}{\partial r} = \frac{1}{rc} H'\left(\frac{U}{U_\tau}\right) \frac{1}{U_\tau}\frac{\partial U}{\partial r} \quad , \quad U_\tau = U_\tau(x) \tag{17}$$

so that

$$U_\tau = \frac{1}{Urc} H'\left(\frac{U}{U_\tau}\right) \frac{\partial U}{\partial r} \tag{18}$$

Integrating U_τ over the area between the wall and radius r

$$\begin{aligned} \int_a^r U_\tau \, r dr &= \frac{1}{c}\int_a^r H'\left(\frac{U}{U_\tau}\right) \frac{1}{U}\frac{\partial U}{\partial r} dr \\ &= \frac{1}{c}\int_0^{U/U_\tau} H'(\gamma)\frac{d\gamma}{\gamma} = G\left(\frac{U}{U_\tau}\right) \end{aligned} \tag{19}$$

so that

$$\frac{1}{2} C U_\tau (r^2 - a^2) = G\left(\frac{U}{U_\tau}\right) \tag{20}$$

Inverting this expression, we obtain

$$\frac{U}{U_\tau} = F\left[\frac{1}{2} C U_\tau (r^2 - a^2)\right] \tag{21}$$

for convenience, we can evaluate the constant C as follows. From Eq. (21)

$$\left(\frac{\partial U}{\partial y}\right)_{y=0} \frac{\tau_w}{\mu} = U_\tau \left\{F\left[\frac{1}{2} C U_\tau (r^2 - a^2)\right] C U_\tau r\right\}_{r=a}$$

or

$$\frac{\tau_w}{\mu} = U_\tau^2 \, C \, a \, F'(0)$$

let $F'(0) = 1$ and then since $\rho U_\tau^2 = \tau$, to obtain $C = 1/a\nu$. Thus, Richmond's law of the wall, which assumes the validity of the two-dimensional streamline hypothesis near the wall beneath an axisymmetric turbulent boundary layer, is

$$\frac{U}{U_\tau} = F\left[\frac{U_\tau}{2a\nu}(r^2 - a^2)\right]$$

or

$$\frac{U}{U_\tau} = F\left[\frac{yU_\tau}{\nu}(1 - \frac{y}{2a})\right] \tag{22}$$

using the new coordinate $\frac{U_\tau y}{\nu}(1 + \frac{y}{2a})$, one can write the two-dimensional law of the wall in the form

$$\frac{U}{U_\tau} = 5.75 \log_{10}\left[\frac{U_\tau y}{\nu}(1 + \frac{y}{2a})\right] + 5.10 \tag{23}$$

where the function F is the usual (empirically verified) form for two-dimensional flow. It appears that the above Eq. (23) provides an adequate representation of our results for $\delta/a \approx 2$. There are indications from Richmond's work (1957), that the region of validity of Eq. (23) becomes a rather small region near the wall as δ/a becomes large.

There are a number of other investigations of the mean flow field in the region near the wall. In the work of Yu (1958) (which includes experimental results) a different method was developed (at Iowa Institute of Hydraulic Research under the guidance of Rouse and Landweber) for correlation of the mean flow in the wall region and the wake region. In Yu's formulation, the wall region contains the free stream velocity as an additional parameter (in addition to the parameters ν, U_τ, and a). We have chosen Richmond's method for data presentation because in the wall region one should not have free stream velocity as a parameter.

Yasuhara (1959), has reported mean velocity measurements on a slender cylinder for cases in which $\delta/a \approx 1$. Yasuhara presented his results in the form advocated by Richmond (1957), with results quite similar to Richmond's and to our present measurements.

Rao (1967) has reported a different form for the law of the wall. His form is derived on the basis that for a slender cylinder, $\delta/a \gg 1$, the sublayer thickness is comparable to the radius of transverse curvature. This reasoning suggests that

$$\frac{U}{U_\tau} = \frac{U_\tau a}{\nu} \ln \frac{r}{a} \tag{24}$$

This form is certainly correct in the sublayer where as Rao points out $r\tau = \text{const} = a\tau_w$. However, we doubt that the sublayer thickness can ever be as large as the radius of curvature of the cylinder. Thus, we believe

that the correct conception of the sublayer is a region dominated by wall effects and that even when a becomes very small the sublayer thickness is always small compared to the radius of curvature of the surface, a. If this were not true, the turbulent eddying flow would wash the fluid in the sublayer (assumed to be of the order of a distance, a, from the wall), completely off the cylinder. The flow in a region occupying a cross-sectional area of the order of the cylindrical cross-sectional area, therefore, cannot be termed a sublayer and Rao's formulation, Eq. (24) cannot be correct. Rao goes on to propose that throughout the boundary layer, the form of the velocity profile should be

$$\frac{U}{U_\tau} = F\left[\frac{U_\tau a}{\nu} \ln \frac{r}{a}\right] \tag{25}$$

where F is the function obtained for the law of the wall in a two-dimensional flow. We have not used this form, Eq. (25), because it has the obvious property (since the function F is a logarithm in the wall region) of taking the logarithm of the logarithm of r/a. This certainly reduces scatter of data points for large r thereby requiring extremely accurate measurements to determine the validity of the formulation, Eq. (25). It would appear that the mean flow field in a turbulent boundary layer with transverse curvature is not well understood when δ/a is large. The law of the wall, Eq. (23), has only a small region of validity and an appropriate similarity law for the wake region has not been firmly established.

C. EXPERIMENTAL RESULTS FOR MEAN FLOW FIELD

1. Pressure Gradient

The streamwise static pressure distribution along the surface of the cylinder at two different free stream velocities was measured as described in Section III. A. The results were plotted in Fig. 10, showing a slight streamwise pressure increase. This was caused by the too rapid divergence of the side walls of the wind tunnel test section. (The original designers over estimated the correction necessary for boundary layer growth on the test section walls). The mean flow field in the flat plate (two-dimensional) boundary layer on the floor of the test section has been investigated by Willmarth and Wooldridge (1962). It was found that in the pressure gradient of Fig. 10, the mean velocity profiles were (within the accuracy of the measurements) those generally accepted for an equilibrium two-dimensional boundary layer, see Coles (1954). In addition, the dimensionless shape factor, Γ, of Buri (see Schlichting (1968)) where

$$\Gamma = \frac{\theta}{U_\infty}\frac{dU_\infty}{dx}\left(\frac{U_\infty \theta}{\nu}\right)^{1/4} = -\frac{\theta}{2}\frac{dC_p}{dx}\left(\frac{U_\infty \theta}{\nu}\right)^{1/4} \qquad (26)$$

was $\Gamma \approx -6 \times 10^{-4}$ or approximately 1/100 of the value, $\Gamma = -7 \times 10^{-2}$, required for separation of a two-dimensional turbulent boundary layer. We can conclude that the slight positive (adverse) pressure gradient $\partial C_p/\partial x = 3 \times 10^{-3}$ ft.$^{-1}$, will not cause the mean flow in the boundary layer to deviate appreciably from the zero pressure gradient case.

2. Skin Friction

The wall shear stress was measured using a Preston tube as described in Section III. A. The results are displayed in Fig. 13 (see also Tables 1 and 2) along with the measurements of Richmond (1957), Yasuhara (1959), and Yu (1958) for axially symmetric turbulent boundary layers with approximately the same ratio of θ/a as our experiments. The present measurements agree reasonably well with previous results at $R_\theta \simeq 10^4$ and extend the skin friction $R_\theta \simeq 3.5 \times 10^4$ for $0.15 < \theta/a < 0.25$. Note that the skin friction coefficient is appreciably larger than in a flat plate turbulent boundary layer. This is qualitatively the same trend that one finds in a laminar boundary layer with transverse curvature.

Because Yu's (1958) definition of θ is different from ours, Eq. (8), when θ is calulated according to Eq. (8), Yu's value of R_θ is reduced by approximately 15%.

3. Velocity Profiles

The velocity profiles measured at the location of the pressure transducers are plotted in Fig. 11 in the form suggested for the law of the wall with transverse curvature, see Eq. (22). The shear velocity U_τ was obtained from skin friction measurements using the relation $U_\tau = (\tau_w/\rho)^{1/2}$. The results of the velocity profile measurements, Fig. 11, show that Richmond's modified law of the wall, Eq. (22), agrees fairly well with measurements of the present investigation for $\delta/a \leq 2$.

Table 1

Summary of Some Results of Skin Friction Measurements

X(ft)	U_∞(fps)	R_a	θ(in.)	θ/a	R_θ	C_f	Source
8	30	15250	0.253	0.253	3860	0.0037	Yu (1958)
8	60	30750	0.247	0.247	7600	0.00338	"
7	90	45060	0.20	0.200	9010	0.00315	"
8	154	40200	0.069	0.138	5540	0.00323	Richmond (1957)
9	154	40200	0.094	0.188	7540	0.00305	"
10	154	40200	0.109	0.210	8750	0.00290	"
3.28	110	21800	0.051	0.154	3360	0.00347	Yasuhara (1959)

X = Distance from the nose of the cylindrical model.

4. Summary of Properties of the Boundary Layer

In Table 2, the various properties of the turbulent boundary layers with transverse curvature that we have measured are summarized.

Table 2

Properties of the Axially Symmetric Turbulent Boundary Layer
Measured in the Present Investigation

x(ft)	U_∞(fps)	R_a	θ(in.)	θ/a	U_τ	C_f	C_f/C_f'	R_θ	$\delta/2a$	δ^*/θ
24	200	134,000	0.382	0.254	6.96	0.00244	1.17	33,800	1.007	1.15
24	145	115,000	0.341	0.228	4.98	0.00232	1.08	26,200	0.926	1.23
24	100	70,200	0.359	0.238	3.83	0.00292	1.30	16,800	1.073	1.14
16	198	136,000	0.218	0.146	7.30	0.00274	1.21	19,800	0.607	1.14
16	101	69,800	0.244	0.162	3.92	0.00301	1.21	11,300	0.80	1.21

C_f' (flat plate) due to Coles (1954).

V. EXPERIMENTAL RESULTS

The measurements of the wall pressure fluctuations beneath the axially symmetric boundary layer will be discussed in the light of our knowledge of wall pressure fluctuations beneath a plane two-dimensional boundary layer. The most striking property of the wall pressure fluctuations beneath a plane boundary layer is the now well known fact that the random pressure fluctuations are convected at speeds of the order of $0.5\ U_\infty$ to $0.85\ U_\infty$. The convection and decay of the pressure fluctuations were first measured by Willmarth (1958) using the technique of space-time correlation in which time delay is varied for a constant separation distance between pressure transducers. The use of space-time correlation measurements in turbulent flow was pioneered by Favre (1952) (who measured the space-time correlation between streamwise velocity fluctuations).

For the present experiment we have found that the space-time correlation of wall pressure fluctuations beneath the boundary layer with transverse curvature also shows convection and decay, but with the important difference that the rate of decay of pressure correlations is more rapid. This will be discussed in detail below along with other statistical measurements of the random pressure field which include the mean-square; power spectrum; lateral, oblique, and longitudinal correlations (with zero time delay); and narrow frequency band correlations

of the wall pressure fluctuations. We will compare our present measurements with the two-dimensional measurements as we proceed with our description.

A. LONGITUDINAL SPACE-TIME CORRELATIONS OF THE WALL PRESSURE

The results of our longitudinal space-time correlation measurements are shown in Fig. 13. The correlation curves (reading from top to bottom) were measured at increasing values of spatial separation. The peaks of the correlation occur at larger and larger time delay as the spatial separation increases (note that the displaced time origins are indicated by small vertical bars on Fig. 13.) At large spatial separations a small peak appeared on the left branch of the curve. This is the upstream propagation of pressure fluctuations caused by sound produced in the wind-tunnel diffuser and fan. The mean-square sound pressure in the test section can be estimated from the average maximum value of the peak on the space-time correlation curve for $\tau < 0$. It is approximately $0.02\ \overline{p^2}$. This value was used in estimating the true value of the spatial correlations of wall pressure. (See Appendix A.)

Qualitatively similar space-time correlations have been measured beneath a plane boundary layer. The essential difference between the present measurements and those in a plane boundary layer is that with transverse curvature the pressure correlation decays more rapidly.

However, in the present investigation, the convection speed is identical (within the experimental error) with the convection speed in a plane boundary layer. Figure 14 shows the location, for various streamwise spatial separations and time delays, of the maxima of the pressure correlation along with the two-dimensional results from Willmarth and Wooldridge (1962) and Bull (1963). Figure 15 shows the convection speed for increasing values of spatial separation. The convection speed of Fig. 15 is obtained graphically from the slope of the locus of the peaks of pressure correlation of Fig. 14. The reader should note that this definition of convection speed is not by any means unambiguous since the correlation of the pressure decays in time and space. A perfectly definite convection speed is easy to define and to understand if one has a convected frozen random pattern convected at constant speed because the lines of constant correlation and the convection path in the x_1, τ plane will be parallel straight lines whose slope is the convection velocity. In the case of a decaying random field in which turbulence of various scales moving at different convection speeds is present, we may refer to Wills (1964) who has discussed the difficulties with the various definitions of convection speed and has proposed a convection speed definition based on a maximum integral time scale that is different from the definition we have used. In practice, for our experiments, it is an almost impossible procedure to use Wills' definition of convection speed since one must measure pressure correlations while

varying the spatial separation between the pressure transducers. * The surface curvature and the inaccessibility of the cylindrical model (in the center of the tunnel) make this impractical. Also, it is not really necessary to use a precise definition of convection velocity because we are looking for changes from the rather well known convection properties of the two-dimensional wall pressure fluctuation field. The definition of convection velocity used for the present work is precisely the same as that used in our previous plane boundary layer experiments.

As we have already mentioned, the convection velocity is the same as that found beneath a plane boundary layer. The measurements show in each case an increase in convection velocity from 0.56 U_∞ to 0.83 U_∞ as the longitudinal spatial separation is increased. The increase in convection velocity is caused by the more rapid decay of the smaller pressure producing eddies near the wall. After the smaller eddies have decayed only larger eddies remain and, since they are larger, their effective centers are farther from the wall and they move at a faster speed owing to the higher mean velocities farther from the wall. The concept of an effective center of such a poorly defined entity as an eddy is admittedly vague. It is more accurate to speak of a convected distribution

---

*Or use numerous closely space transducers.

of vorticity which if of large scale (therefore, extending into the higher speed regions of the boundary layer) must move at a higher average speed than a small scale distribution of vorticity near the wall.

Although the convection speeds in the plane and axially symmetric boundary layer are the same there are important differences between the space-time correlation for the two cases. In the boundary layer with transverse curvature, the rate of decay of the maximum of the space-time correlation is more rapid than it is in the plane boundary layer. Referrring to Fig. 13, we see that when $x_1/\delta^* = 9.33$ the maximum pressure correlation is $R_{pp} = 0.1$. In the case of the plane boundary layer, Willmarth and Wooldridge (1962), $R_{pp} = 0.1$ occurs for $x_1/\delta^* = 22.6$. The decay of the maximum (or peak) value of the pressure correlations for plane and axially symmetric boundary layers are shown in Fig. 16, where $R_{pp}(x_1, 0, \tau_c)$ is the peak value of the pressure correlation. From the figure, it can be observed that in the boundary layer with transverse curvature, the decay of pressure correlations is faster than it is in a plane boundary layer. Note that the decay rate is especially rapid at small spatial separations. For large spatial separations the rate of decay (the slope of curves in Fig. 16) is approximately the same. We will discuss these matters in more detail after we have presented all the experimental results. Additional measurements of convection speeds have been obtained from space-time correlation measurements with $x_3 \neq 0$. These are discussed in Appendix B.

B. LONGITUDINAL, LATERAL AND OBLIQUE SPATIAL CORRELATIONS OF THE WALL PRESSURE

The spatial correlations of the wall pressure (with zero time delay) have been studied in considerable detail to determine the contours of constant pressure correlation on the surface of the cylinder. The array of thirteen pressure transducers, see Fig. 7, was designed so that a large number of pressure correlations for different spatial separations could be efficiently measured with a small number of pressure transducers. All of the wall pressure correlations were measured in the frequency band $0.144 < \frac{\omega\delta^*}{U_\infty} < 28.8$, and have been corrected for effect of sound in the free stream. (See Appendix A.)

The results of the spatial correlation measurements are displayed in Fig. 17, 18, 19, and 20. Consider Fig. 17 and 18 which show the longitudinal and lateral pressure correlation. It is clear that the pressure correlation decreases with x_1 or x_3 more rapidly than has been observed in the plane boundary layer. For the present case of a boundary layer with transverse curvature in which $\delta/a \simeq 2$, the lateral or longitudinal spacing at which any given positive value of the pressure correlation is attained is the order of half the spacing at which the same value of pressure correlation is attained in the plane boundary layer.

Figures 19 and 20 show measurements of spatial correlation in oblique directions, along a 45^o line in Fig. 19 and for various oblique locations in Fig. 20. In all these measurements, using the array of

transducers of Fig. 7, we have assumed that the random wall pressure field is statistically homogeneous. Thus, we ignore the rather slow streamwise changes in the statistical structure of the wall pressure field. This means that the pressure field is homogeneous longitudinally

$$R_{pp}(x_1, x_3, 0) = R_{pp}(-x_1, x_3, 0) \tag{27}$$

and by axial symmetry laterally homogeneous

$$R_{pp}(x_1, x_3, 0) = R_{pp}(x_1, -x_3, 0) \tag{28}$$

Therefore, the number of wall pressure correlations measurements necessary is reduced. (Actually it is sufficient to measure correlations in only one quadrant of the x_1, x_3 surface.)

The results of all the measurements of pressure correlation with zero time delay are summarized and compared with the plane boundary layer case in Fig. 21 and 22, respectively.

Figure 21 shows that the contours of constant pressure correlation are very nearly circular and that the correlation has decayed with distance to 1/20 of the maximum value in a distance of approximately 1.5 δ^*. (Note that in this experiment $\delta^* = 0.42$ inches and $\delta = 2.8$ inches.) In the lateral direction, a distance $x_3 = 1.5\,\delta^*$ corresponds to only 23.7 degrees of arc along the cylinder. Note that in Fig. 18, the lateral pressure correlation is negligibly small for $x_3/\delta^* \geq 6.2$ and does not appear to

oscillate. We do not expect that appreciable correlation of the wall pressure (relative to the value of $R_{pp} = 0.05$ at $x_3/\delta^* = 1.5$) for points on opposite sides of the cylinder would be found. Note that we have filtered out all pressure fluctuations with a frequency less than 100 Hz and, since the convection speed is of the order of $0.8\ U_\infty$, the half wave length of the pressure fluctuations that have been rejected is already quite large, that is, greater than or equal to $1/2(0.8\ U_\infty/100\ \text{Hz}) \simeq 7$ inches (or 2.5δ). Recall that the pressure correlation is essentially zero in a distance of the order of $3\delta^* \simeq 0.5\ \delta$.

Figure 22 compares the contours of constant correlation for plane and axially symmetric boundary layers. The iso-correlation contours in the axially symmetric boundary layer are nearly circular as compared to the case of the plane boundary layer in which the larger iso-correlation contours, for smaller values of R_{pp}, are elongated in the transverse, x_3, direction. For large values of R_{pp} (small size iso-correlation contours) the shape of the iso-correlation contours is nearly circular for both the plane and axially symmetric boundary layer.

From these results it is apparent that the effect of transverse curvature is to reduce the scale of all the random pressure producing eddies by a factor of two or more for $\delta/a \approx 2$. The reduction in transverse scale of the larger eddies is greater than the longitudinal scale reduction. But for the smaller eddies, the scale reduction is approximately the same in the longitudinal and transverse directions.

C. ROOT-MEAN-SQUARE WALL PRESSURE

The root-mean-square (rms) value of the pressure fluctuations on the surface of a cylinder was measured in the frequency band $0.063 < \frac{\omega\delta^*}{U_\infty} < 57.6$. The measurements are compared with the rms wall-pressure associated with plane boundary layer obtained by other investigators in Table 3. The present data has been corrected for free stream sound. * According to Bull (1963), the ratio rms wall-pressure to free stream dynamic pressure is not dependent on Reynolds number. But the ratio of rms wall-pressure to skin friction increases slightly when Reynolds number increases. In the later case, the increase occurs because the skin friction coefficient decreases as Reynolds number increases. If we compare the ratios $\sqrt{\overline{p^2}/q_\infty}$ or $\sqrt{\overline{p^2}/\tau_\omega}$ for the plane and axially symmetric boundary layers, see Table 3, we find that there is not a large change in either ratio caused by transverse curvature. For instance, if we compare the values listed in Table 3, the uncorrected ratio of rms wall-pressure to dynamic pressure beneath an axially symmetric boundary layer increases 9% from the value measured by Willmarth and Roos (1965) at slightly higher Reynolds number. Recalling that transverse curvature increases the mean skin friction, we note that transverse curvature decreases the ratio $\overline{p^2}/\tau_w$ by approximately 10%. In any case, there is not a large effect of transverse curvature on the root-mean-square wall pressure for $\delta/a \leq 2$.

---

*See Appendix A.

Table 3

Comparison of Root-Mean-Square Values of the Wall Pressure Fluctuations

	$\sqrt{\overline{p^2}/q_\infty}$	$\sqrt{\overline{p^2}/\tau_w}$	R_θ	Frequency Range	Remarks	
Axially Symmetric Boundary Layer	5.6×10^{-3}	2.26	26,200	$0.063 < \omega\delta^*/U_\infty < 57.6$	Uncorrected	Present data
	5.99×10^{-3}	2.42	26,200	$0.063 < \omega\delta^*/U_\infty < 57.6$	Corrected	$R/\delta^* = 0.072$
Plane Boundary Layer	5.14×10^{-3}	2.54	38,000	$0.14 < \omega\delta^*/U_\infty < 28.8$	Uncorrected	Willmarth and Roos (1965) $R/\delta^* = 0.061$
	5.64×10^{-3}	2.66	38,000	$0.14 < \omega\delta^*/U_\infty < 28.8$	Corrected	
	5.35×10^{-3}	2.48	19,500	$0.016 < \omega\delta^*/U_\infty < 19.9$	Corrected	Bull (1963)
	5.45×10^{-3}	2.58	26,000	$0.087 < \omega\delta^*/U_\infty < 11$	Corrected	
	5.4×10^{-3}	2.80	33,800	$0.14 < \omega\delta^*/U_\infty < 17$	Corrected	

D. POWER SPECTRUM OF THE WALL PRESSURE

The power spectrum of the wall pressure fluctuations beneath the axially symmetric turbulent boundary layer measured with the present pressure transducers ($R/\delta^* = 0.072$) at $U_\infty = 145$ ft/sec was obtained in the frequency range from 100 to 20,000 Hz ($0.144 \leq \frac{\omega\delta^*}{U_\infty} \leq 28.8$). The data were compared with the power spectrum in the plane boundary layer measured with a pressure transducer with $R/\delta^* = 0.061$ by Willmarth and Roos (1965) and with a pressure transducer with $R/\delta^* = 0.095$ by Bull (1963), see Fig. 23. The reason for choosing 100 Hz as the lower frequency limit for our measurements was the possibility of free stream temperature and vorticity distrubances caused by heat input or cooling at the wall of the wind tunnel circuit. A description of our observations of this phenomenon are given in Willmarth and Wooldridge (1962). However, in the present investigation, we did not observe the severe pressure disturbances at low frequencies that were found at the wall, Willmarth and Wooldridge (1962). The reason may be that the effects of external heat input or cooling remain confined to a region near the wind tunnel wall. Generally speaking, the shape of the wall pressure spectra beneath a two-dimensional boundary layer and beneath a boundary layer with transverse curvature do not appear greatly different on a log-log plot. However, on closer examination one finds that at high frequencies, $\omega\delta^*/U_\infty > 10$, the wall pressure spectrum beneath the boundary layer with transverse

curvature contains approximately twice the energy density that was measured beneath a plane boundary layer and at low frequencies, $\omega\delta^*/U_\infty < 1$, the energy density of the pressure spectrum beneath the boundary layer with transverse curvature is 75% less than beneath a plane boundary layer. The normalized power spectra are shown on a linear scale in Fig. 25. It is quite clear on the linear scale that there is, indeed, greater spectral density at high frequencies. The data of Fig. 25 have been corrected for the effects of attenuation caused by the finite size of the pressure transducer. This is discussed below.

E. CORRECTIONS FOR FINITE TRANSDUCER SIZE

Experimental resolution of the structure of the turbulent pressure field is limited by the finite size of the pressure transducer. For a transducer of diameter 2R, the measurements of the spectrum of the pressure at a frequency of the order of $U_\infty/2R^*$ or greater will be subject to a considerable error which becomes larger as the frequency increases. Therefore, it is desirable to use as small a diameter transducer as possible. In the present investigation, the diameter of the transducer was 0.06 inches and the frequency $U_\infty/2R$ was 30 Hz. (Note that most of the energy in the spectra of Fig. 23 occurs at frequencies less than 20 KHz.) Therefore, the present results should not be subject to a large error.

---

*This is the frequency for which the transducer diameter equals the wave length and for a one-dimensional pressure field and a transducer there would be a complete cancellation of the pressure signal at this frequency.

Corrections to the power spectrum measured by a finite size transducer have been computed by Corcos (1963). His calculations assume that the pressure field can be represented as a function of the variables $\omega x_1/U_c$ and $\omega x_3/U_c$. For this reason and others, related to his method of calculation, his corrections are an approximation to the true corrections. His approximate corrections agree very well with our experimental results and calculations, Willmarth and Roos (1965), when $\omega R/U_c < 1$.

We have used Corcos' (1963) computations for the correction of our power spectrum beneath the boundary layer with transverse curvature because $\omega R/U_c < 1$ in the range of interest for our spectrum. Note that using Corcos' computations means that the wall pressure must be expressible using the similarity variables and functions used by Corcos (1963). To a reasonable approximation this is true and is discussed in Appendix C. The corrected power spectrum non-dimensionalized by rms wall-pressure is presented on a logarithmic scale in Fig. 24 and on a linear scale in Fig. 25. For comparison, the corrected dimensionless power spectrum of the plane boundary layer wall pressure measured by other investigators are also presented in the figures.

The corrected root-mean-square wall-pressure is listed in Table 3. Note that the correction to the root-mean-square wall-pressure is not more than 10%.

F. INTEGRAL SPATIAL AND TEMPORAL SCALES

The integral scales of the wall pressure were computed according to the formulae

$$\Lambda_1 = \int_{-\infty}^{\infty} |R_{pp}(x_1, 0, 0)| \, dx_1 \tag{29}$$

$$\Lambda_3 = \int_{-\infty}^{\infty} |R_{pp}(0, x_3, 0)| \, dx_3 \tag{30}$$

$$\Lambda_\tau = \int_{-\infty}^{\infty} |R_{pp}(0, 0, \tau)| \, d\tau \tag{31}$$

where Λ_1, Λ_3, and Λ_τ are respectively the longitudinal, lateral and temporal integral scale. We have used the absolute value of pressure correlation in our definitions to ensure that spuriously small integral scales are not produced by oscillations of the pressure correlation caused by the rejection of low frequencies when the signals were filtered.

The various integral scales are collected for comparison with the case of a plane boundary layer in Table 4. It is apparent that in all cases the effect of lateral transverse curvature is to reduce the spatial and temporal integral scales. It is clear and not too surprising that transverse curvature reduces the lateral integral scale, Λ_3, by a larger amount (a factor of 2.5 or more) than the reduction of the longitudinal and temporal scales (a factor of the order of 1.5).

Table 4

Integral Spatial and Temporal Scale in Plane and Axially Symmetric Turbulent Boundary Layer

	Axially Symmetric Boundary Layer	Plane Boundary Layer	
Frequency Range	$0.144 < \frac{\omega\delta^*}{U_\infty} < 28.8$	$0.14 < \frac{\omega\delta^*}{U_\infty} < 13.6$	$0.075 < \frac{\omega\delta^*}{U_\infty} < 7.5$
$\tau_\Lambda U_\infty/\delta^*$	2.92	3.90	3.84
Λ_1/δ^*	1.31	2.06	3.20
Λ_3/δ^*	1.04	2.51	6.74
Remarks		Willmarth and Wooldridge (1962)	Bull (1963)

VI. SUMMARY AND DISCUSSION

From the results of our measurements presented in Section V and in Appendix C, we can make a qualitative assessment of the effect of transverse curvature on the structure of turbulence and on the wall pressure.

First consider the result of Fig. 14 and 15 which show that the convection speed in the boundary layer with transverse curvature is almost the same as in a plane boundary layer. Next, consider the velocity profiles in the two boundary layers which are compared in Fig. 26 where the displacement thickness, δ^*, has been used as a length scale. We have used δ^* exclusively for our length scale in presenting our results because it is a more definite quantity than δ and has been successfully used in the case of the plane boundary layer. (As a matter of fact, our qualitative discussion would not be changed if θ or δ were used as the characteristic length.) From Fig. 26, it is apparent that the velocity profile is much "fuller" when transverse curvature is present. Consider a turbulent pressure producing eddy near the wall of any given size (relative to δ^*). It is clear that if an eddy of this given size is present in a boundary layer with transverse curvature, it will have a higher convection velocity than it would have in a plane boundary layer, (because at every point in the eddy the mean velocity would be larger). On the other hand, as mentioned above, the measured convection velocity in the two

boundary layers is nearly the same. The explanation for the unchanged convection velocity is that the pressure producing eddies in the boundary layer with transverse curvature must be smaller and therefore nearer the wall where the mean velocity is lower.

The assertion that the pressure producing eddies are smaller (relative to δ^*) in a boundary layer with transverse curvature is in agreement with all our other measurements.

Consider the relative size of the contours of constant pressure correlation of Fig. 22. In a boundary layer with transverse curvature, the contours are smaller, by approximately a factor of two or more, than they are in a plane boundary layer. Figure 16 shows the decay of the peaks of longitudinal space-time correlation. The decay is much more rapid at small spatial separation in a boundary layer with transverse curvature* and this is caused by the presence of smaller eddies that are created by the transverse curvature. (Recall that Willmarth and Wooldridge (1962) have shown that an eddy of any given size decays after traveling a distance proportional to its size.) Thus, if there are relatively more smaller

---

* Note that in Fig. 16 for $x_1/\delta^* > 6$ the rate of decay of the maxima of the pressure correlation in the plane and axially symmetric boundary layer is the same. This indicates that after the smaller eddies have decayed, the eddy size distribution of larger eddies is similar.

eddies, they will decay in a shorter distance. Finally, the power spectrum of the wall pressure (see Fig. 24) contains a greater energy density at high frequencies than in a plane boundary layer owing to the unchanged convection speed of smaller eddies.

Consider now the shape of the contours of constant correlation in a plane boundary layer for $R_{pp} \leq 0.1$. (See Fig. 22.) The contours for $R_{pp} \leq 0.1$ are larger transversally than in the stream direction. However, the smaller contours for larger R_{pp} ($R_{pp} \geq 0.3$) are nearly circular. In a boundary layer with transverse curvature all the contours are smaller and nearly circular. We believe that there are two primary effects in a boundary layer with moderate transverse curvature that reduce the size of turbulent eddies. The first effect which causes a reduction in size of the eddies is the increased fullness of the velocity profile. * The turbulent eddies near the wall moving at any given convection speed are necessarily smaller because the mean velocity corresponding to that speed is reached at a point nearer the wall. In addition, there is a second effect in which the larger eddies suffer a greater reduction in transverse scale than small eddies because the wall is curved transversely. Thus, if one visualizes a large eddy adjacent to the curved wall, it is apparent that in the transverse direction at either side of

---

* See the discussion of Section I about the effect of transverse curvature on the mean velocity profile.

the periphery of a large eddy the mean velocity is higher than it would be at the sides of the same eddy in a plane boundary layer. Thus, there is a streamwise shearing motion along the sides of large eddies in a boundary layer with transverse curvature that is not present in a plane boundary layer. This shearing motion acts to reduce the transverse scale of large eddies. *

Additional confirmation for the above selective effect of transverse curvature on the lateral scale of large pressure producing eddies is contained in Appendix C. There, the effect of transverse curvature on the decay of the narrow band correlation of the pressure in a lateral direction is to cause a more rapid decay for large eddies (in a low frequency band) than it is for small eddies (in a high frequency band).

---

*If we consider the extreme case of large transverse curvature with $\delta/a \to 0$, the transverse extent of the largest eddy is limited to a distance of the order of 2δ. For a plane boundary layer there is no readily apparent limiting transverse length.

APPENDIX A

CORRECTION OF WALL PRESSURE FOR THE EFFECT OF SOUND IN THE FREE STREAM

The pressure measured at the wall is

$$p_m = p + p_s$$

where p is the turbulent wall pressure and p_s is the pressure produced by sound waves in the free stream. Define the true value of the wall pressure correlation as

$$(R_{pp})_t = \frac{\overline{p_1 p_2}}{\overline{p^2}}$$

The measured pressure correlation is

$$(R_{pp})_m = \frac{\overline{(p_1 + p_s)(p_2 + p_s)}}{\overline{(p + p_s)^2}} = \frac{(R_{pp})_\tau + \overline{p_s^2}/\overline{p^2}}{1 + \overline{p_s^2}/\overline{p^2}}$$

where assume $\overline{p_1^2} = \overline{p_2^2}$ and $\overline{p_1 p_s} = \overline{p_2 p_s} = 0$

Therefore

$$(R_{pp})_t = (1 + \overline{p_s^2}/\overline{p^2})(R_{pp})_m - \overline{p_s^2}/\overline{p^2} \qquad (32)$$

For Willmarth and Wooldridge's (1962) data $\overline{p_s^2}/\overline{p^2} = 0.05$ and

$$(R_{pp})_t = 1.05\,(R_{pp})_m - 0.05 \tag{33}$$

For the present data $\overline{p_s^2}/\overline{p^2} = 0.02$ and

$$(R_{pp})_t = 1.02\,(R_{pp})_m - 0.02 \tag{34}$$

APPENDIX B

CONVECTION SPEEDS MEASURED IN OBLIQUE DIRECTIONS

From the results of oblique ($x_3 \neq 0$) space-time correlation measurements, the locus of the peaks of pressure correlation were plotted in Fig. 27 as a function of longitudinal spatial separation for several obliquities (various values of x_3/δ^*). Figure 27 shows that the location of the peaks of the pressure correlation in the x_1, τ plane remains the same as it was for $x_3 = 0$. Thus, the decay of the wall pressure in the transverse direction does not directly effect the convection speed in the longitudinal direction.

APPENDIX C

CORRELATION OF THE WALL PRESSURE IN NARROW FREQUENCY BANDS

Let $p(x, z, t; \omega)$ be the signal obtained by passing the output of a pressure transducer at (x, z) through an ideal filter which has a narrow pass band centered at a frequency, ω, whose width is $\Delta\omega$. Then the correlation of pressure fluctuations measured by two pressure transducers a distance (x_1, x_3) apart at central frequency ω for a band width $\Delta\omega$ is

$$Q'_{pp}(x_1, x_3, \tau; \omega) = \frac{1}{T} \int_0^T p(x, z, t; \omega)\, p(x + x_1,\ z + x_3, t + \tau; \omega)\, dt \qquad (35)$$

Corcos (1962) has shown that*

$$Q'_{pp}(x_1, x_3, \tau; \omega) = |\Gamma(x_1, x_3, \omega)| \cos(\omega\tau + \alpha)\, \Delta\omega \qquad (36)$$

where $\Gamma(x_1, x_3, \omega) = |\Gamma(x_1, x_3, \omega)| e^{i\alpha}$ is the temporal cross-spectral density of the wall pressure fluctuations and α is the argument of the complex quantity Γ. The cross-spectral density is related to the spectrum by

$$\Gamma(x_1, x_3, \omega) = \frac{1}{4\pi^2} \iint_{-\infty}^{\infty} E(k_1, k_3, \omega) \exp(k_1 x_1 + k_3 x_3)\, i\, dk_1\, dk_3 \qquad (37)$$

---

*See Bull (1961) for a complete discussion.

The narrow band correlation coefficient is defined as

$$R'_{pp}(x_1, x_3, \tau;\omega) = \frac{Q'_{pp}(x_1, x_3, \tau, i, \omega)}{Q'_{pp}(0, 0, 0;\omega)} \tag{38}$$

Corcos (1962) suggested that Γ could be represented by the expression

$$\Gamma(x_1, x_3, \omega) = |\phi(\omega)| \, A\left(\frac{\omega x_1}{U_c}\right) B\left(\frac{\omega x_3}{U_\infty}\right) \exp\left(\frac{i\omega x_1}{U_c}\right) \tag{39}$$

where $A(\omega x_1/U_c)$ and $B(\omega x_3/U_\infty)$ are functions to be determined experimentally with properties $A(0) = B(0) = 1$ and the convection velocity $U_c = U_c(\omega)$ is function of the central frequency ω. Then

$$Q'_{pp}(x_1, x_3, \tau;\omega) = |\phi(\omega)| \, A\left(\frac{\omega x_1}{U_c}\right) B\left(\frac{\omega x_3}{U_\infty}\right) \cos\left(\omega\tau - \frac{\omega x_1}{U_c}\right) \Delta\omega \tag{40}$$

and

$$Q'_{pp}(0, 0, 0;\omega) = |\phi(\omega)| \, \Delta\omega \tag{41}$$

Therefore, the correlation coefficient in a narrow frequency band at a central frequency ω is

$$R'_{pp}(x_1, x_3, \tau;\omega) = A\left(\frac{\omega x_1}{U_c}\right) B\left(\frac{\omega x_3}{U_\infty}\right) \cos\left(\omega\tau - \frac{\omega x_1}{U_c}\right) \tag{43}$$

The narrow-band longitudinal space-time correlation is

$$R'_{pp}(x_1, 0, \tau, \omega) = A\left(\frac{\omega x_1}{U_c}\right) \cos\left(\omega\tau - \frac{\omega x_1}{U_c}\right) \tag{44}$$

Where the function $A(\omega x_1/U_c)$ is obtained when $\tau = \tau_c = x_1/U_c$

$$A\left(\frac{\omega x_1}{U_c}\right) = |R'_{pp}(x_1, 0, \tau;\omega)| = |R'_{pp}(x_1, 0, \tau_c;\omega)| \tag{45}$$

The narrow-band transverse space-time correlation is

$$R'_{pp}(0, x_3, \tau;\omega) = B\left(\frac{\omega x_3}{U_\infty}\right) \cos \omega \tau \tag{46}$$

The function $B(\omega x_3/U_\infty)$ is obtained with $\tau = 0$

$$B\left(\frac{\omega x_3}{U_\infty}\right) = R'_{pp}(0, x_3, 0;\omega) \tag{47}$$

Relatively narrow-band correlations of the wall pressure were measured in the four frequency bands

$0.61 < \frac{\omega\delta^*}{U_\infty} < 0.97$ Central frequency at $\frac{\omega\delta^*}{U_\infty} = 0.79$

$1.28 < \frac{\omega\delta^*}{U_\infty} < 2.76$ " " " " 2.02

$3.87 < \frac{\omega\delta^*}{U_\infty} < 6.25$ " " " " 5.06

$5.21 < \frac{\omega\delta^*}{U_\infty} < 15.63$ " " " " 10.42

To carry out those measurements two Krohn-Hite model 310-AB variable band-pass filters were used. The high and low pass settings of the two filters were carefully matched to give identical phase shift as a function of frequency so that they were identical (within $\pm 3^{o}$).

From the measured space-time correlation curves, values of correlation amplitude and convection speed were obtained. Figure 28 shows the convection speed for increasing values of spatial separation in various frequency bands. The convection speed of Fig. 28 is obtained in the same way as that described in Section V. A. For an ideally narrow frequency band ($(\Delta\omega/\omega) \ll 1$) the convection speed would remain constant when spatial separation increased. However, Fig. 28 shows an increase in convection speed as the longitudinal spatial separation increased. This is because we have a finite band width and the smaller eddies in that band width decay faster than the larger ones. (See Section V. A). The asymptotic values of convection speed at large spatial separation were plotted in Fig. 29 as a function of dimensionless frequency $\omega\delta^*/U_\infty$. Comparing Fig. 29 with Willmarth and Wooldridge's (1962) data shows that the asymptotic convection speed (i. e., $x_1/\delta^* \to \infty$) of given size eddy in axially symmetric boundary layer is almost identical to that obtained in the plane boundary layer.

The amplitude function $A(\omega x_1/U_c)$ of the narrow-band longitudinal correlation of Corcos' representation can be found by plotting the measured maximum amplitude of space-time correlation, i. e., $R_{pp}(x_1, 0, \tau_c; \omega)$, for various spatial separations and central frequencies (Fig. 30). Figure 30 shows that the amplitude of narrow-band longitudinal space-time correlation is only slightly less than in the plane boundary layer. This means the rate of decay of a given size eddy is about the same as in the plane boundary layer and that the rate of decay is proportional to the size of the eddy.

The amplitude of transverse correlation in Corcos' representation, $B(\omega x_3/U_\infty)$, was obtained by plotting the measured transverse correlations at zero time delay as a function of $\omega x_3/U_\infty$, (see Fig. 31). The measurements show that the amplitude of narrow band transverse correlation for $(x_3/\delta^*) = 0.191$ is nearly the same as in plane boundary layer. But for $(x_3/\delta^*) \geq 0.722$, the transverse correlations fall off very much more rapidly than they do in a plane boundary layer as $\omega x_3/U_\infty$ increases. This means that one effect of the transverse curvature of the wall is to cause an increase in the decay of eddies in transverse direction. This has been discussed in Section V.

The amplitude of narrow-band space-time correlation measured along a line at an angle of 45^o to the stream direction are plotted against $\omega x_1/U_c$ in Fig. 32. The data are compared with computations from Eq. (43)

using the experimentally determined values of $A(\omega x_1/U_c)$ and $B(\omega x_3/U_\infty)$ of Fig. 30 and 31. That is,

$$|R_{pp}(x_1, x_3, \tau;\omega)| = |R_{pp}(x_1, 0, \tau;\omega)| \times |R_{pp}(0, x_3, \tau, \omega)| = A\left(\frac{\omega x_1}{U_c}\right) B\left(\frac{\omega x_3}{U_\infty}\right) \tag{48}$$

This relation appears to give a good approximation to the measured values provided the value of $B(\omega x_3/U_\infty)$ appropriate to the large or small spatial separation x_3/δ^* is used. * This is apparently an effect caused by transverse curvature since a single function $B(\omega x_3/U_\infty)$ suffices for a plane boundary layer. Actually, the formulation of Eq. (40) is only an approximation even for the plane boundary layer and does break down in that case also; see Bull (1963) who showed that for very low frequencies $A(\omega x_1/U_c)$ and $B(\omega x_3/U_\infty)$ were not unique.

---

*Clearly a failure of the formulation of Eq. (40).

REFERENCES

1. Alexander, L. G., Baron, T. and Comings, E. W., (1953), "Transport of Momentum, Mass and Heat in Turbulent Jets," University of Illinois Engineering Experiment Station, Bulletin, Series No. 413.

2. Bull, M. K., (1961), "Space-Time Correlations of the Boundary Layer Pressure Field in Narrow Frequency Bands," University of Southampton Report A. A. S. U. No. 200.

3. Bull, M. K., Wilby, J. F. and Blackman, D. R., (1963), "Wall Pressure Fluctuations in Boundary Layer Flow and Response of Simple Structures to Random Pressure Fields," University of Southampton Report A. A. S. U. No. 243; also Journal of Fluid Mechanics, Vol. 28, 1967, p. 719.

4. Clauser, F. H., (1956), "The Turbulent Boundary Layer," Advances in Applied Mechanics, Vol. 4, Academic Press, p. 1.

5. Coles, D., (1954), "The Problem of the Turbulent Boundary Layer," ZAMP, Vol. 5, p. 181.

6. Coles, D., (1955), "The Law of the Wall in Turbulent Shear Flow," 50 Jahre Grenzshichtforschung, (ed. by Görtler and Tollmien), F. Vieweg und Sohn, Braunschweig, p. 153.

7. Corcos, G. M., (1962), "Pressure Fluctuations in Shear Flows," University of California, Institute of Engineering Research, Report Series No. 183, Issue No. 2; also Journal of Fluid Mechanics, Vol. 16, 1964, p. 353.

8. Corcos, G. M., (1963), "Resolution of Pressure in Turbulence," Acoustical Society of America Journal, Vol. 35, p. 192.

9. Favre, A. J., Gaviglio, J. J. and Dumas, R., (1952), "Some Measurements of Time and Space Correlation in Wind Tunnel," 8th International Congress on Theoretical and Applied Mechanics, Istanbul; also NACA Tech. Memo. 1370 (1955).

10. Glauert, M. B. and Lighthill, M. J., (1955), "The Axisymmetric Boundary Layer on a Long Thin Cylinder," Royal Society of London, Proceedings, Series A, Vol. 230, p. 188.

11. McMillian, F. A., (1954), "Viscous Effects on Flattened Pitot Tubes at Low Speeds," Journal of the Royal Aeronautical Society, Vol. 58, p. 837.

12. Preston, J. H., (1954), "The Determination of Turbulent Skin Friction by Means of Pitot Tubes," Journal of the Royal Aeronautical Society, Vol. 58, p. 109.

13. Rao, G. N. V., (1967), "The Law of the Wall in a Thick Axisymmetric Trubulent Boundary Layer," Journal of Applied Mechanics, Transaction of ASME, Vol. 34, p. 237.

14. Reid, R. O. and Wilson, W., (1963), "Boundary Flow Along a Circular Cylinder," Journal of Hydraulic Division, Proceeding of ASCE, Vol. 89, p. 21.

15. Richmond, R. L., (1957), "Experimental Investigation of Thick Axially Symmetric Boundary Layer on Cylinders at Subsonic and Hypersonic Speeds," Guggenheim Aeronautical Laboratory, California Institute of Technology, Hypersonic Research Project Memo, No. 39.

16. Schlichting, H., (1968), Boundary Layer Theory, 6th ed., McGraw-Hill Book Company, Inc., p. 629.

17. Schloemer, H. H., (1966), "Effects of Pressure Gradients on Turbulent Boundary-Layer Wall-Pressure Fluctuations," U. S. Navy Underwater Sound Laboratory Report, No. 747; also, Acoustical Society of America, Journal, Vol. 42, 1967, p. 93.

18. Smith, D. W. and Walker, J. H., (1958), "Skin Friction Measurements in Incompressible Flow," NACA Tech. Notes - 4231.

19. Tu, B. J. and Willmarth, W. W., (1966), "An Experimental Study of the Structure of Turbulence Near the Wall Through Correlation Measurements in a Thick Turbulent Boundary Layer," University of Michigan, Technical Report, 02920-3-T.

20. Willmarth, W. W., (1958a), "Space-Time Correlation of the Fluctuating Wall Pressure in a Turbulent Boundary Layer," Journal of Aeronautical Sciences, Vol. 25, p. 335.

21. Willmarth, W. W., (1958b), "Small Barium Titanate Transducer for Aerodynamic or Acoustic Pressure Measurements," The Review of Scientific Instruments, Vol. 29, p. 218.

22. Willmarth, W. W. and Wooldridge, C. E., (1962), "Measurements of the Fluctuating Pressure at the Wall Beneath a Thick Turbulent Boundary Layer," Journal of Fluid Mechanics, Vol. 14, p. 187.

23. Willmarth, W. W. and Roos, F. W., (1965), "Resolution and Structure of the Wall Pressure Field Beneath a Turbulent Boundary Layer," Journal of Fluid Mechanics, Vol. 22, p. 31.

24. Wills, J. A. B., (1964), "On Convection Velocities in Turbulent Shear Flows," Journal of Fluid Mechanics, Vol. 20, p. 417.

25. Yasuhara, M., (1959), "Experiments on Axisymmetric Boundary Layers Along a Long Cylinder in Incompressible Flow," Transactions of the Japan Society of Aerospace Sciences, Vol. 2, p. 72.

26. Yu, Y. S., (1958), "Effect of Transverse Curvature on Turbulent-Boundary-Layer Characteristics," Journal of Ship Research, Vol. 2, No. 3, p. 33.

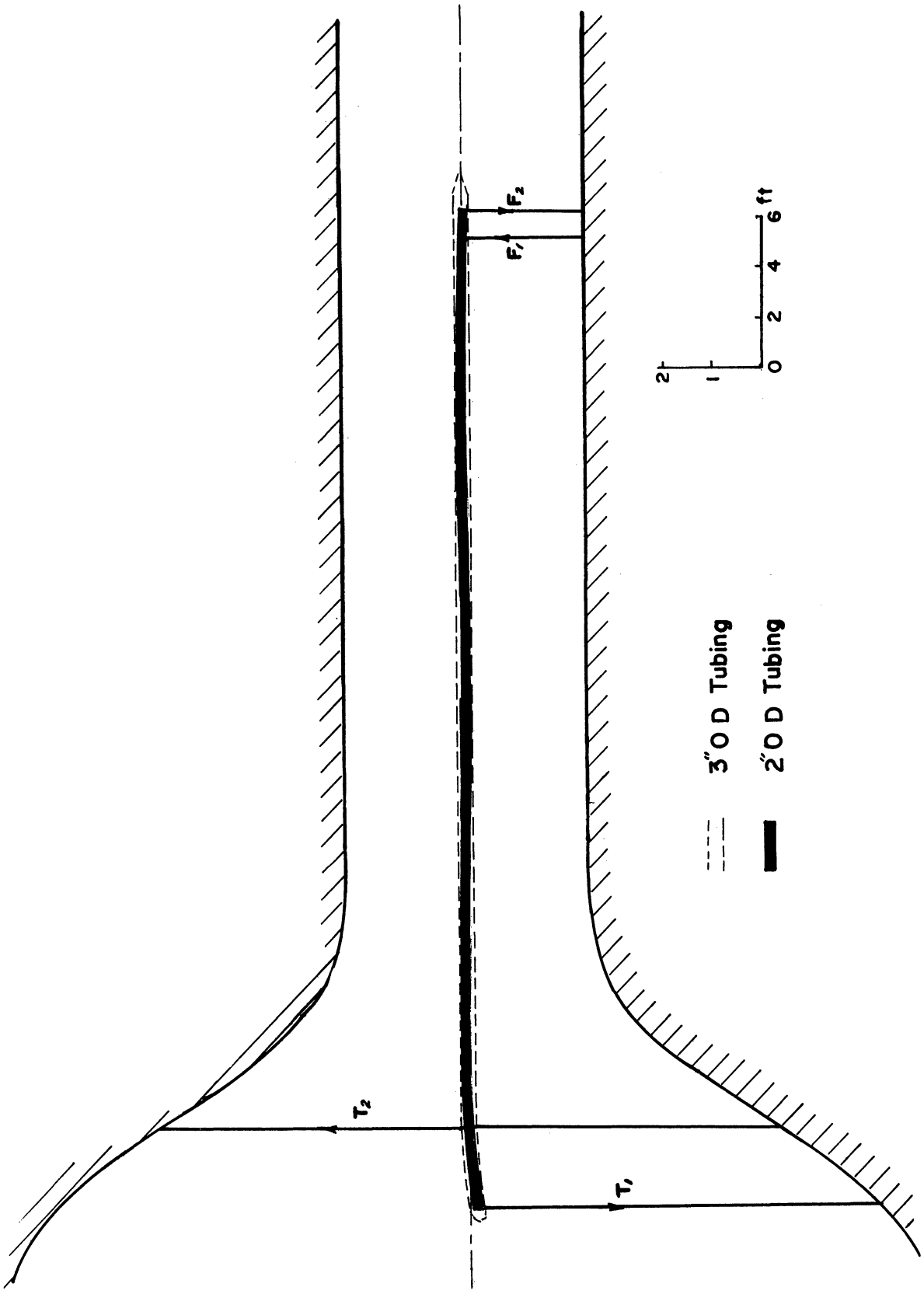

Figure 1. Schematic diagram of 2 in. diameter steel tubing installed in the wind tunnel as the backbone of the cylindrical model.

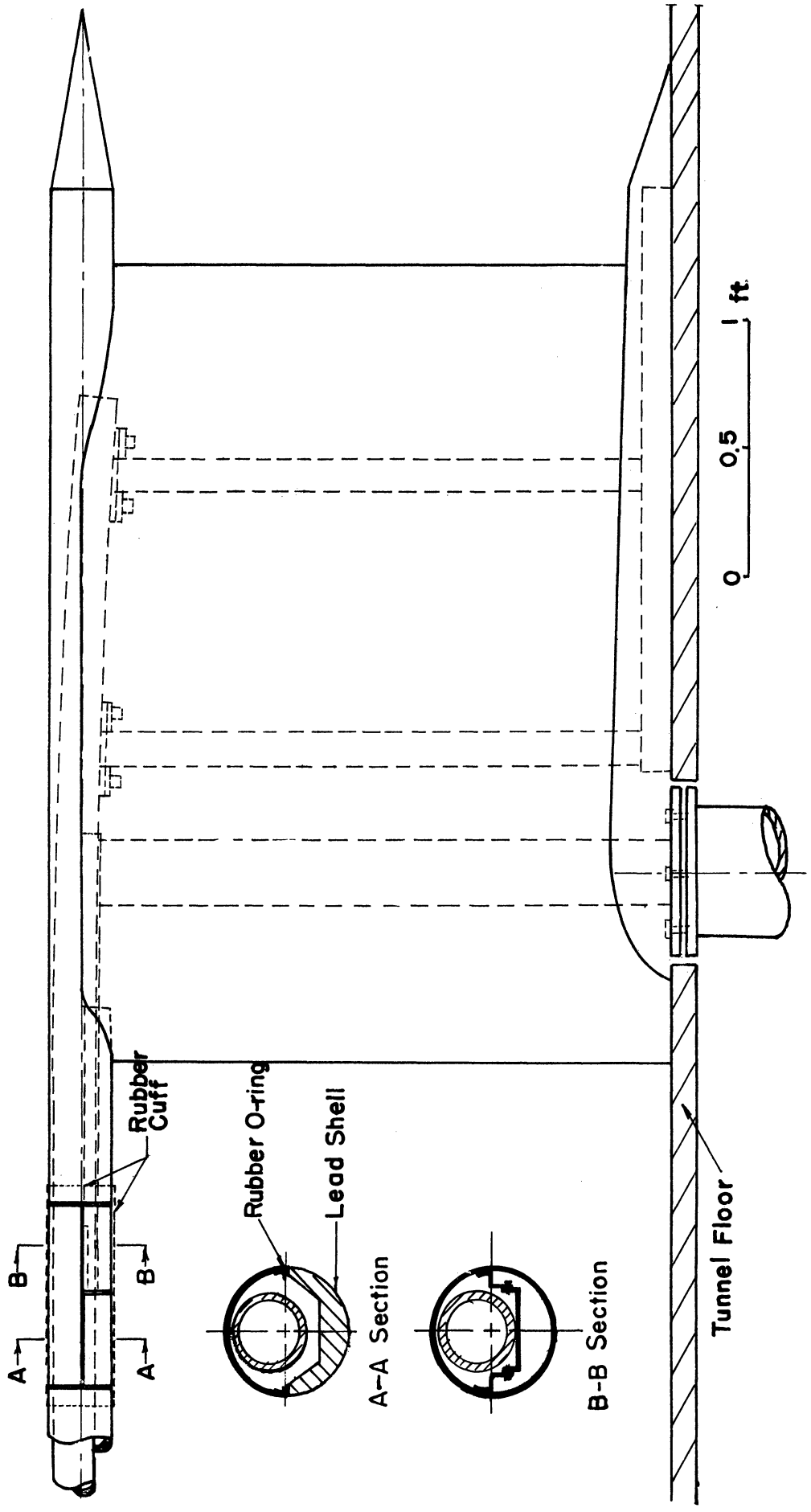

Figure 2. The test station and the rear support of the cylindrical model.

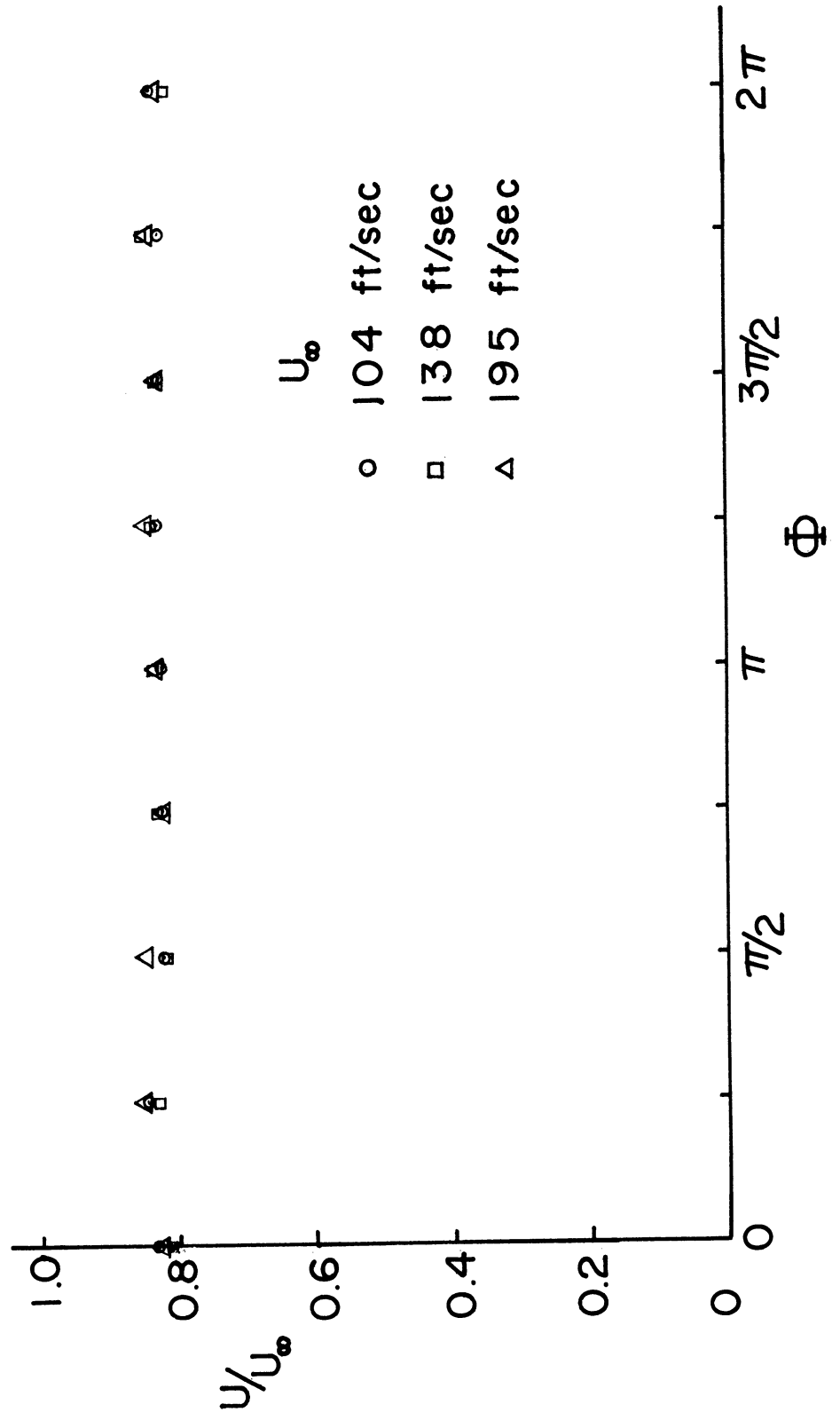

Figure 3. The symmetry of the velocity around the cylinder at y = 0.65 in.

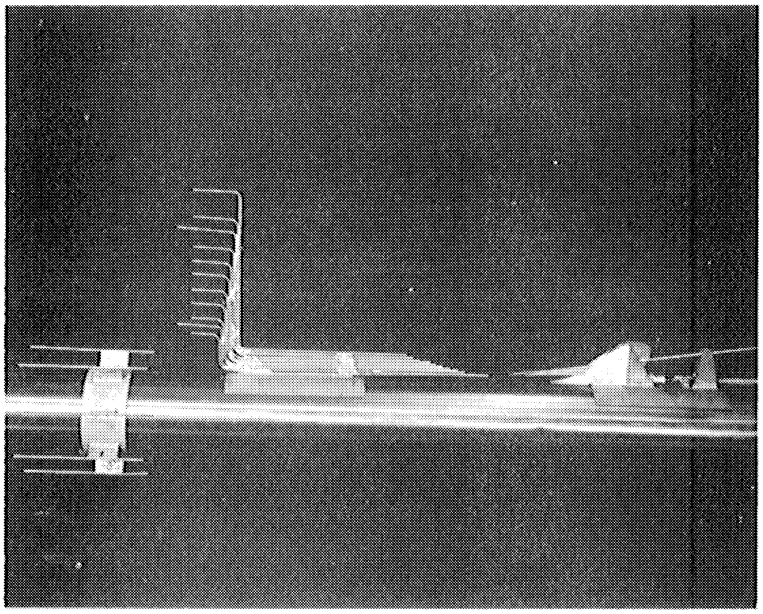

Figure 4. Velocity-survey apparatus.

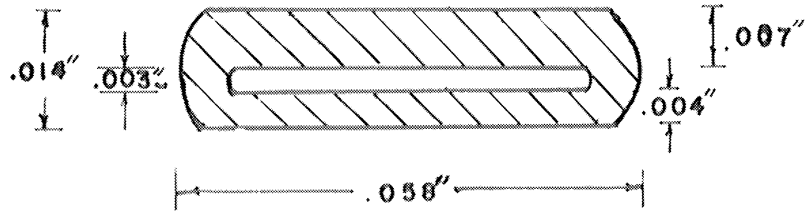

Figure 5. Mouth of the pitot tube.

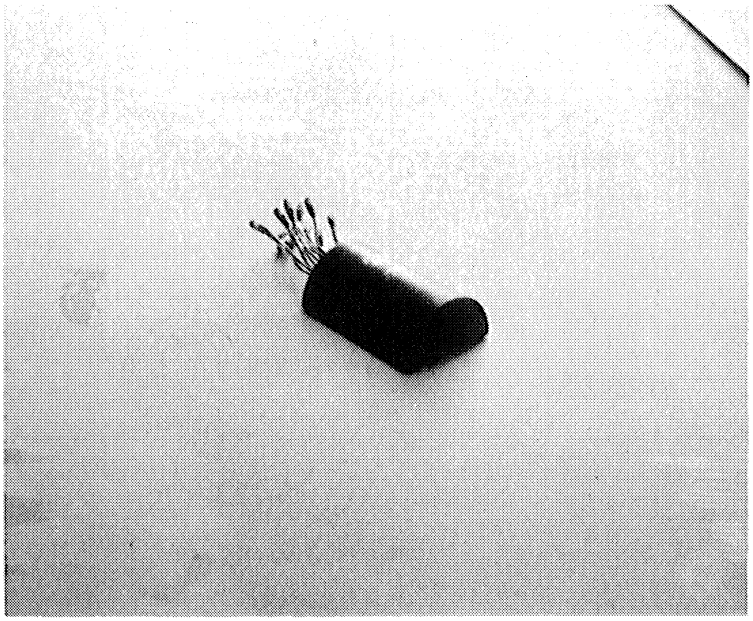

Figure 6. Pressure transducers mounted in the semi-cylinder lead shell.

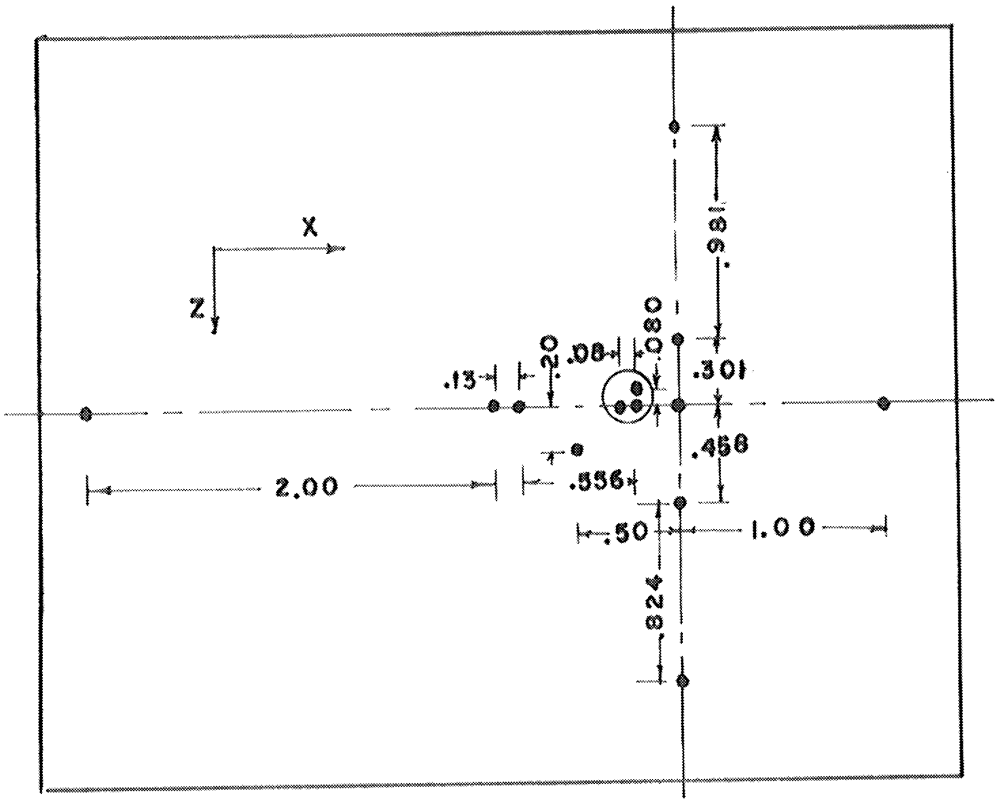

Figure 7. The arrangement of the pressure transducers.

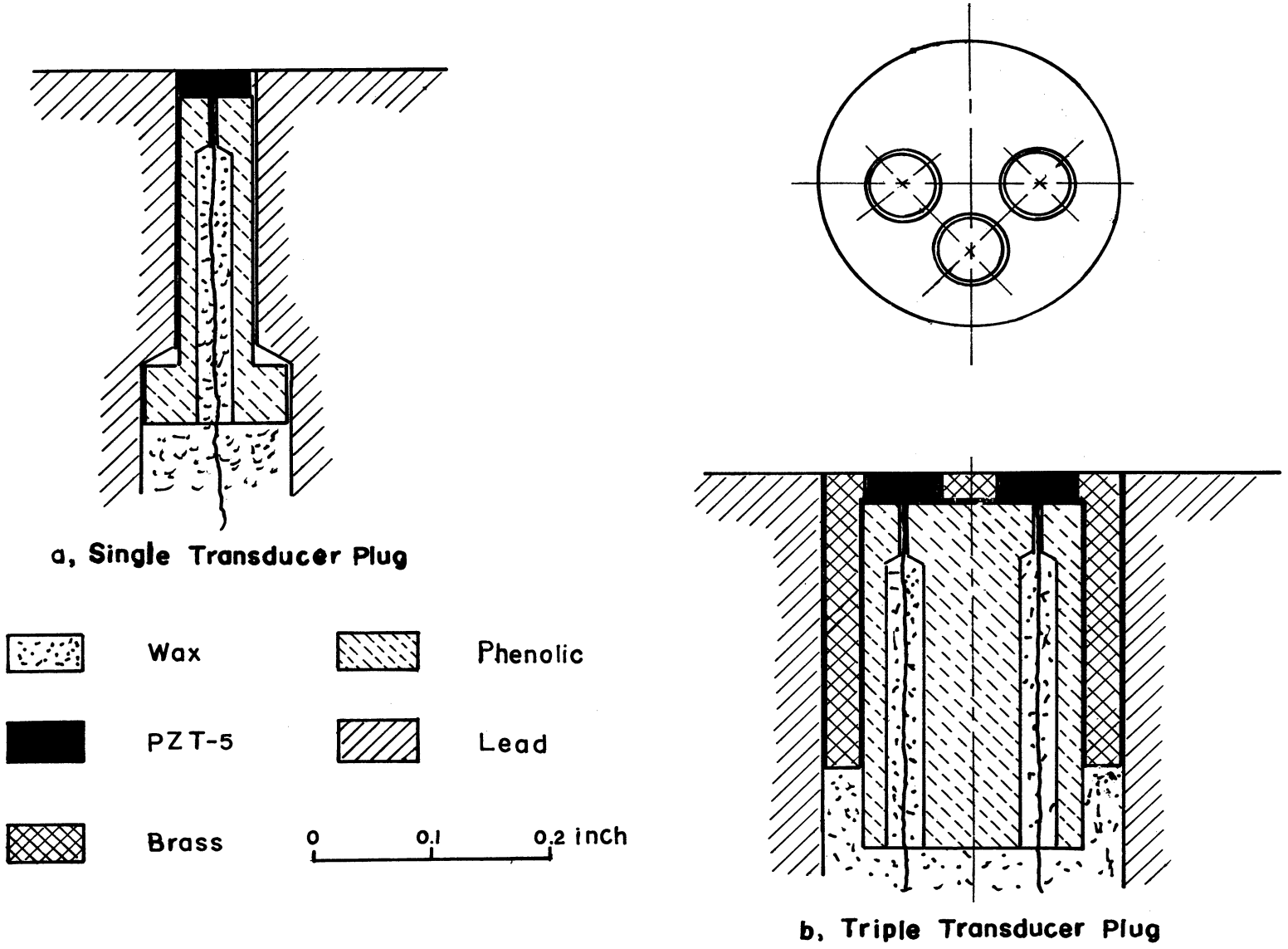

Figure 8. Pressure transducers assembly.

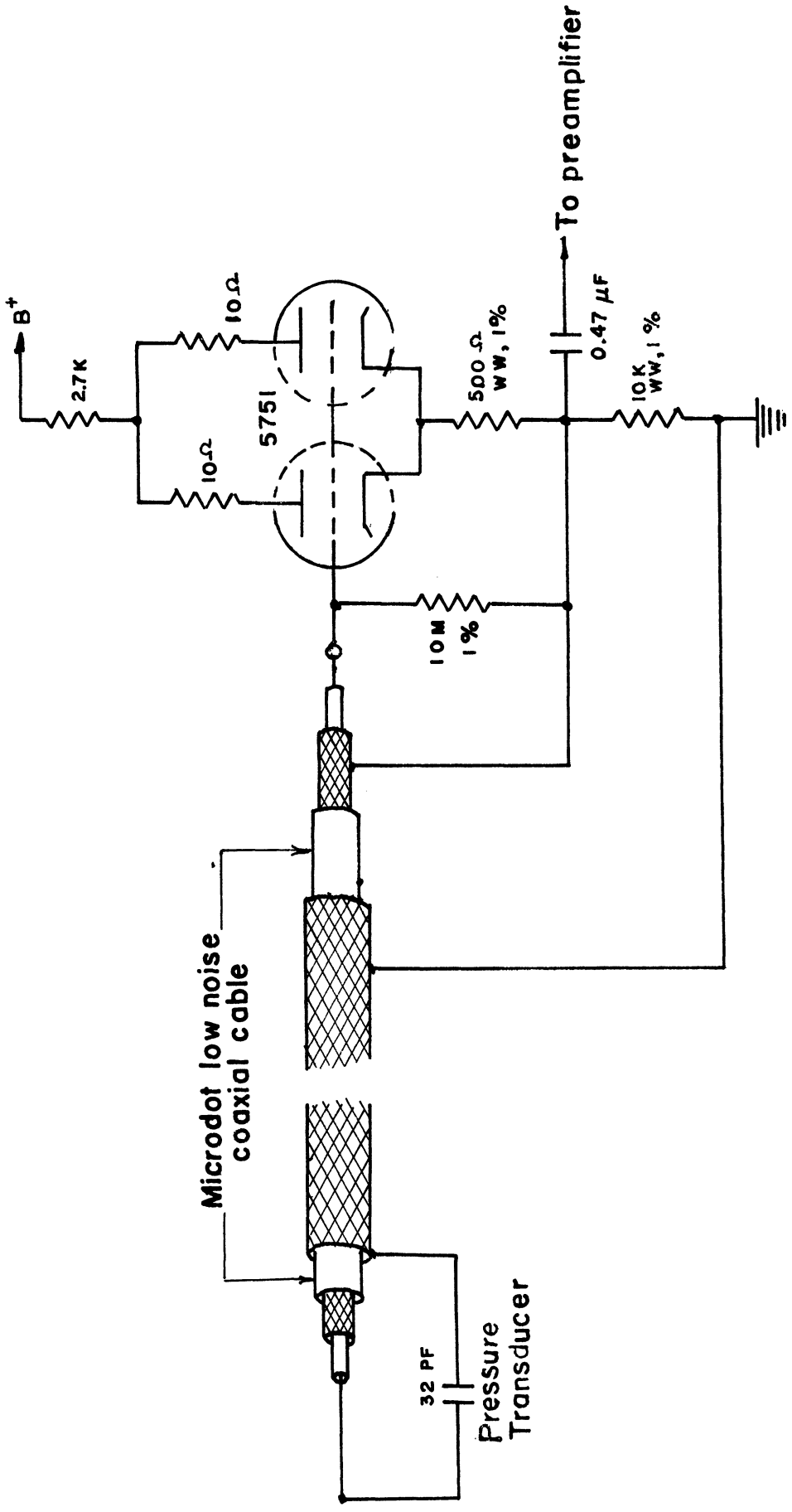

Figure 9. Circuit diagram for pressure transducers and cathode follower.

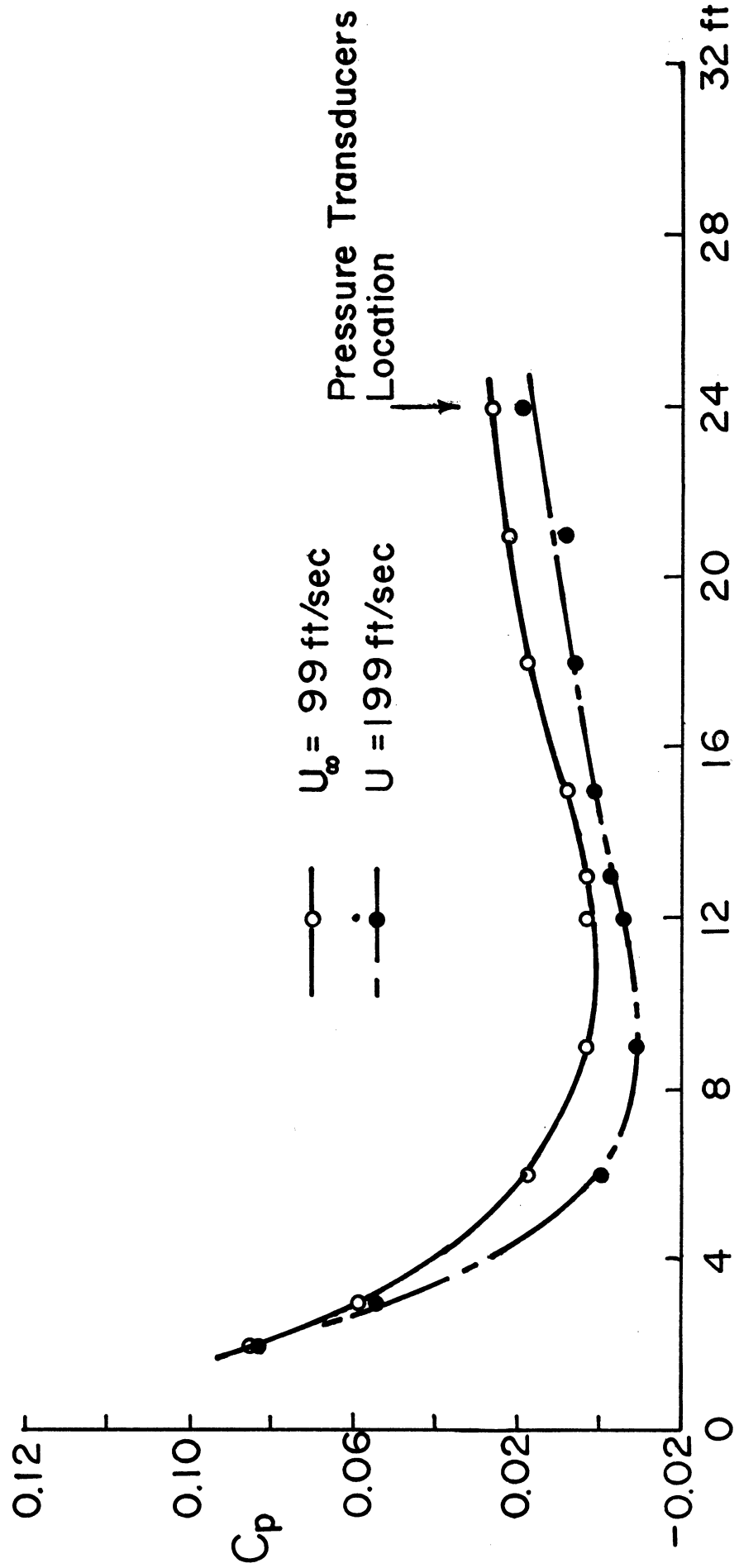

Figure 10. Pressure gradient along the cylinder.

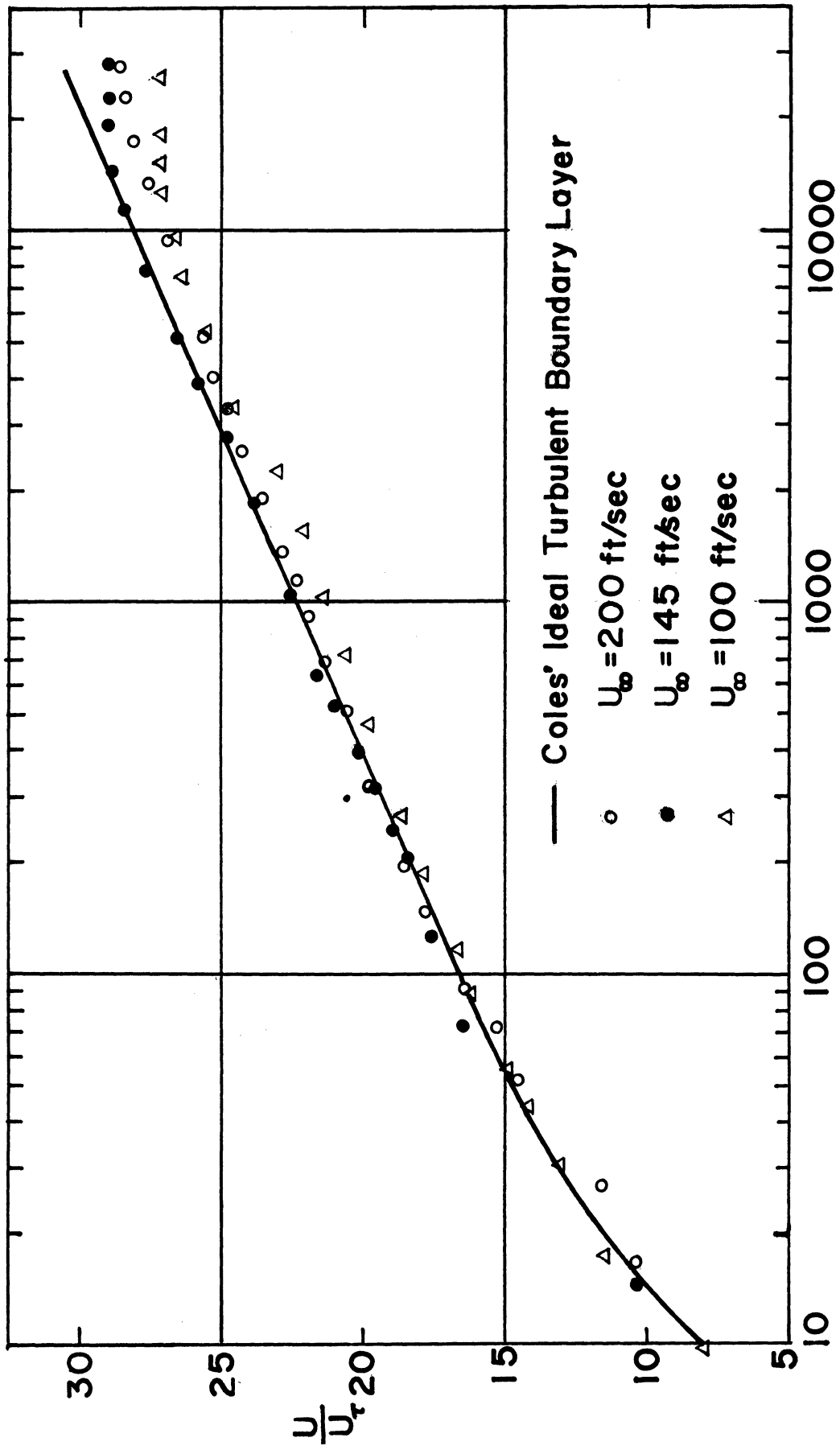

Figure 11. Mean velocity profiles in the axially symmetric turbulent boundary layer (Law of the Wall).

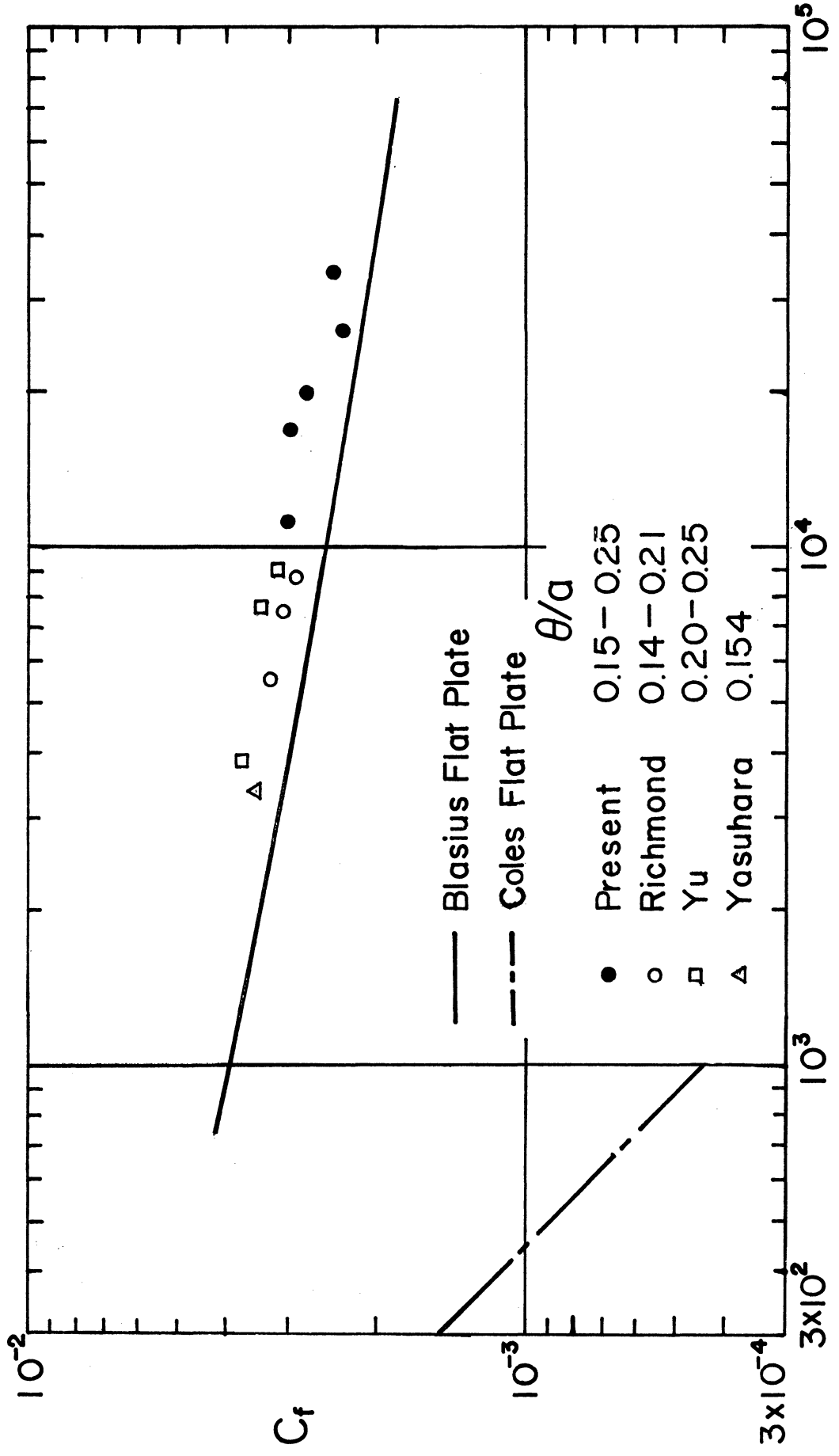

Figure 12. Skin friction coefficient.

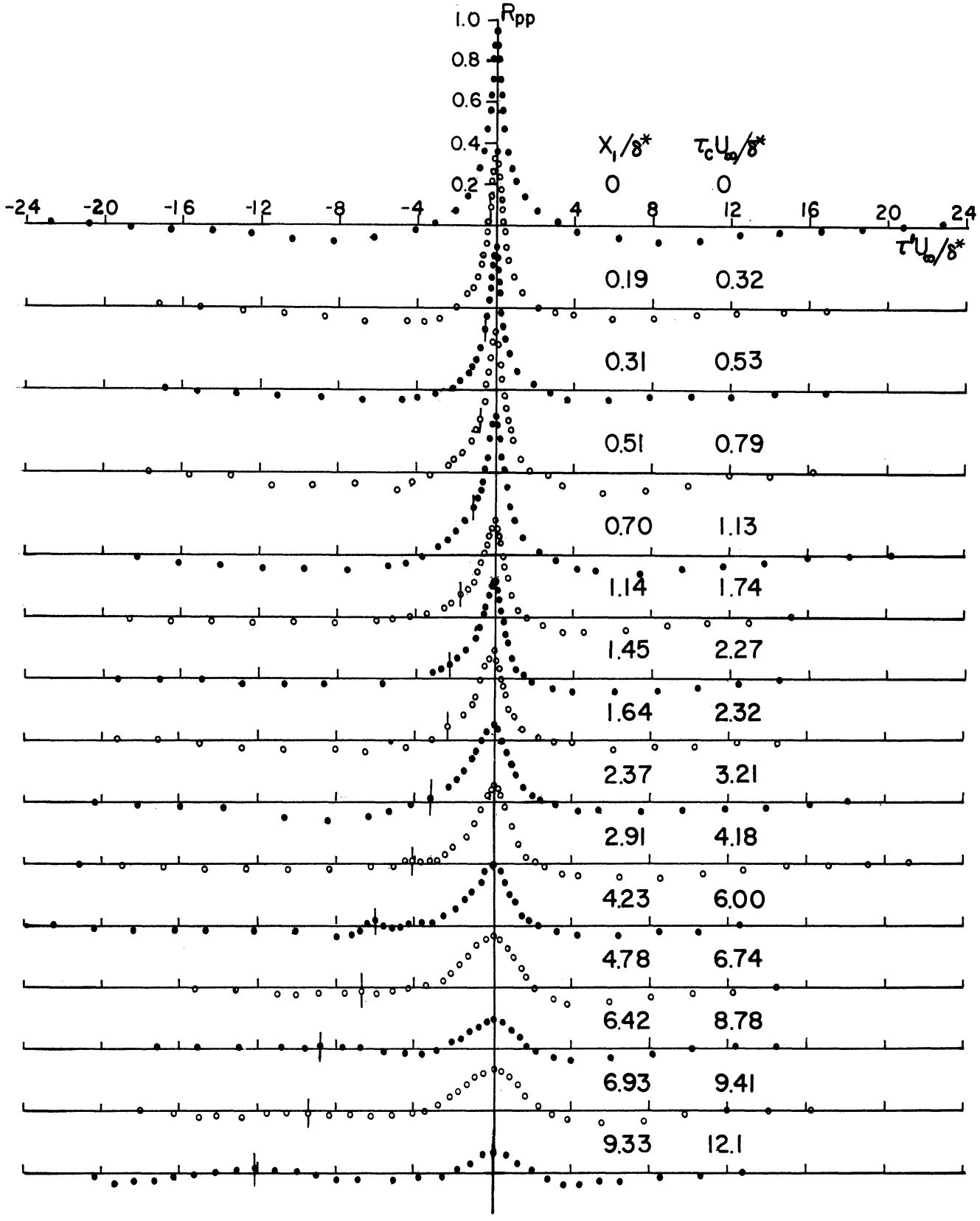

Figure 13. Longitudinal space-time correlation of wall pressure.

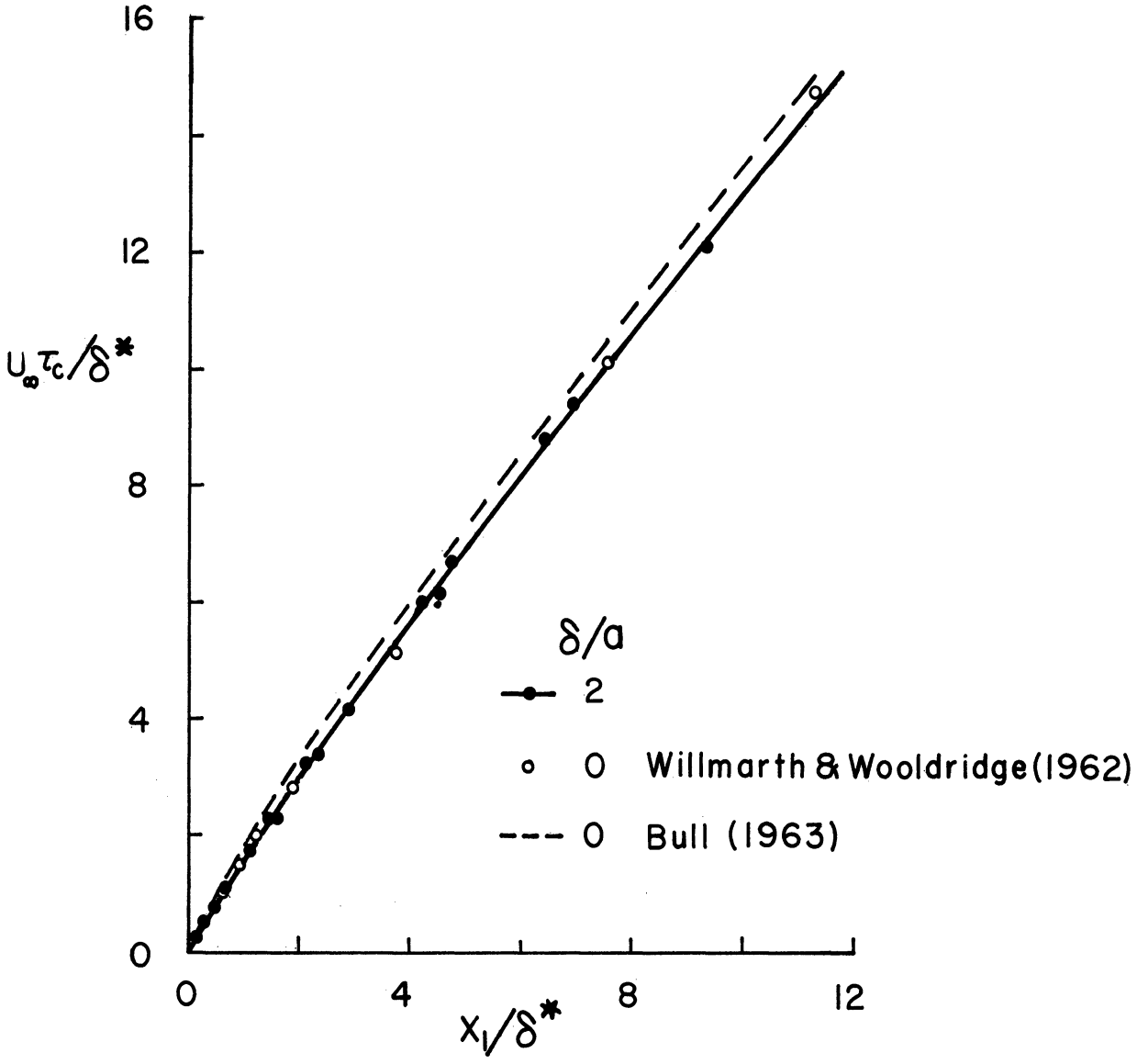

Figure 14. Time delay for R_{pp} maximum at constant x_1.

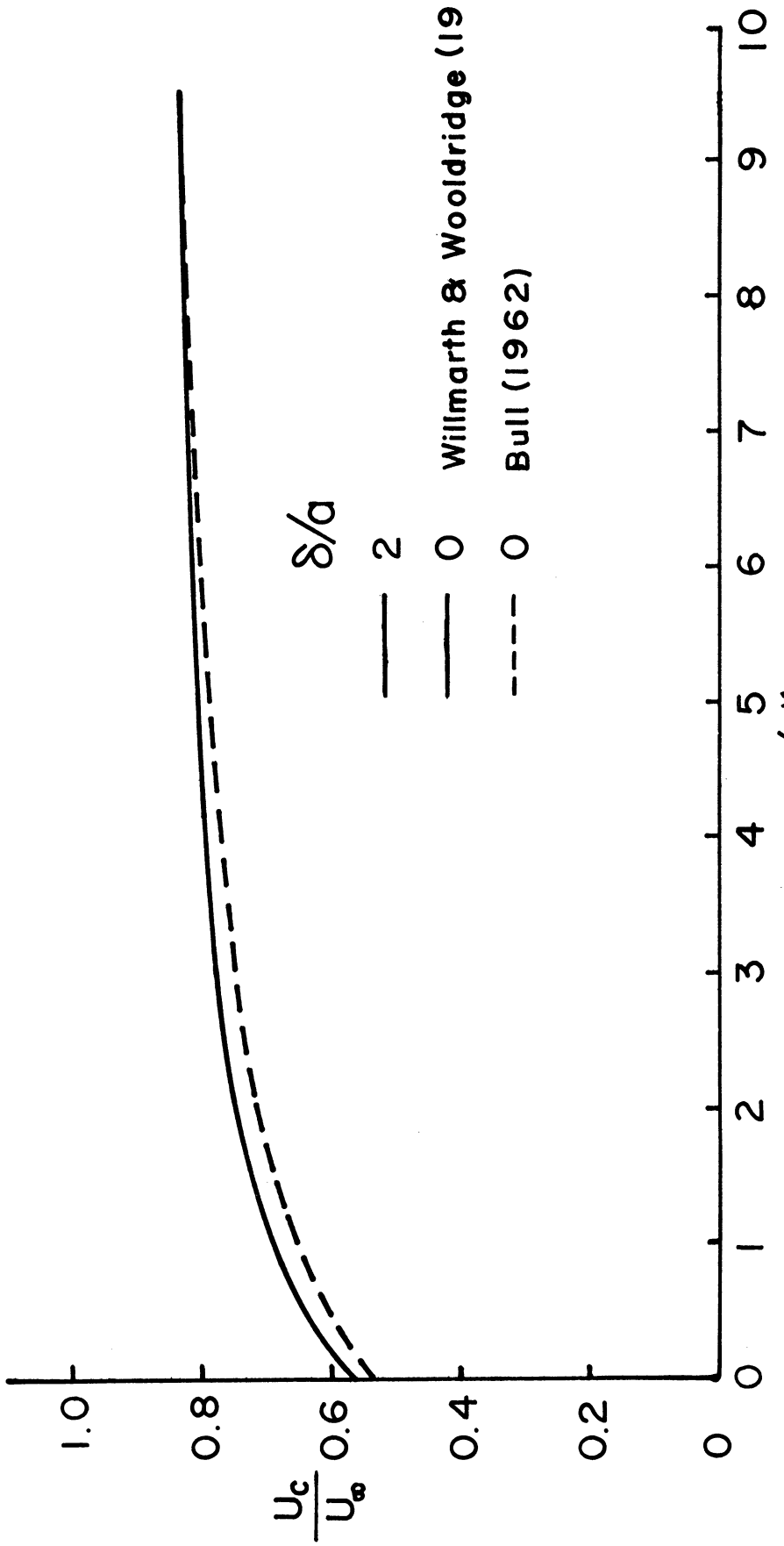

Figure 15. Local convection speed of the pressure-producing turbulent eddies.

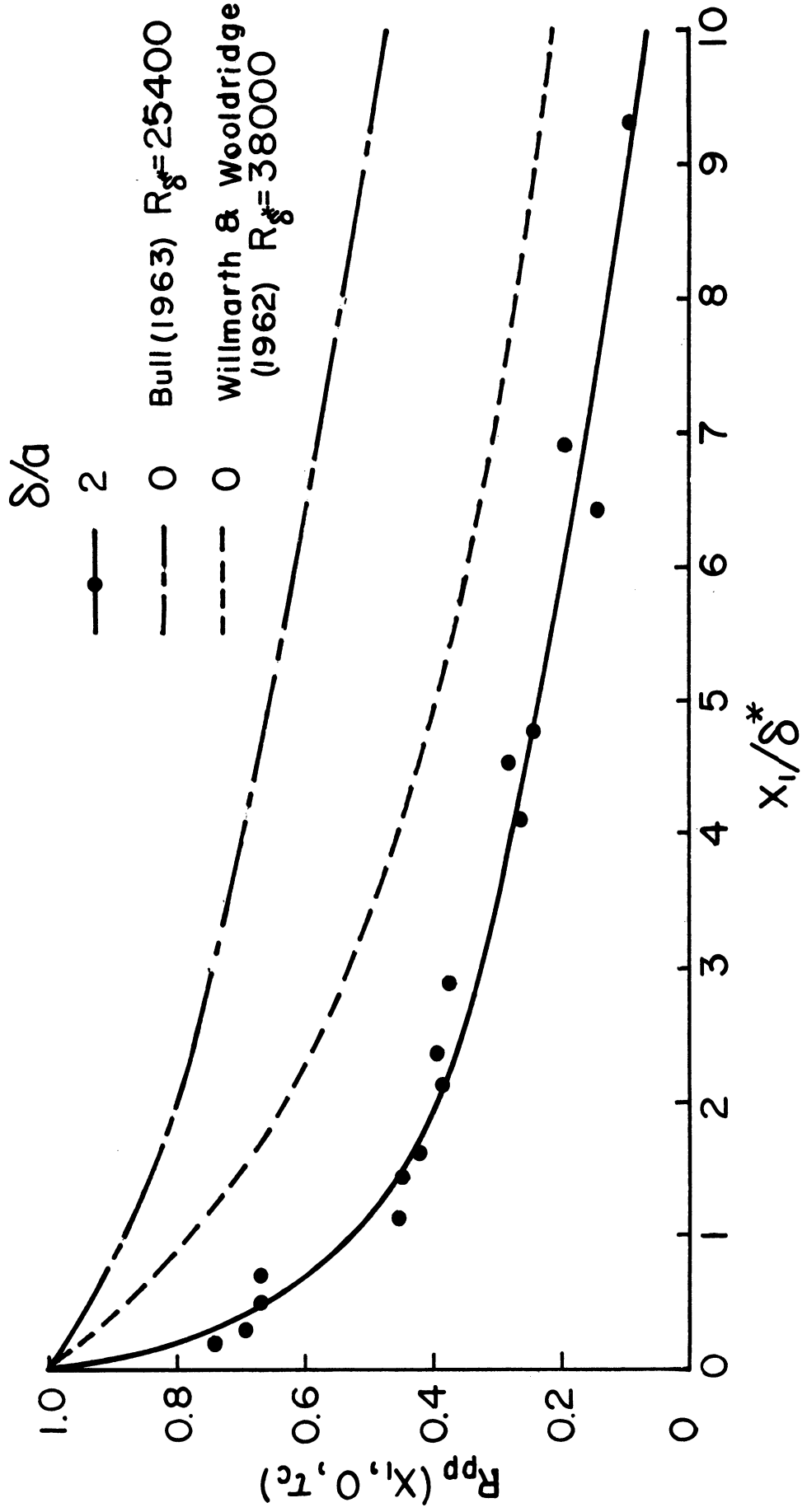

Figure 16. Decay of wall pressure correlation in a reference frame moving at local convection speed.

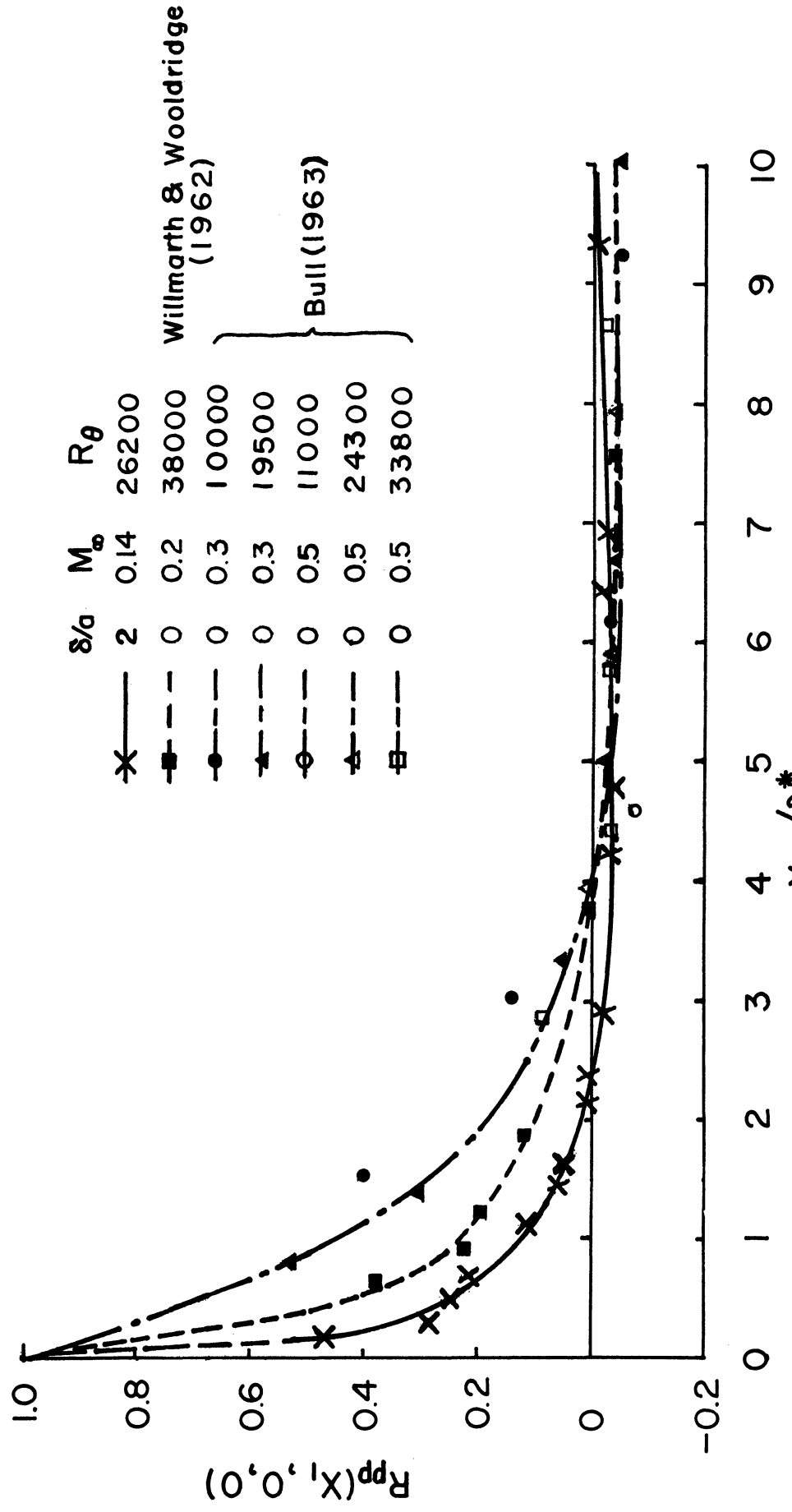

Figure 17. Longitudinal wall pressure correlation in a broad frequency band.

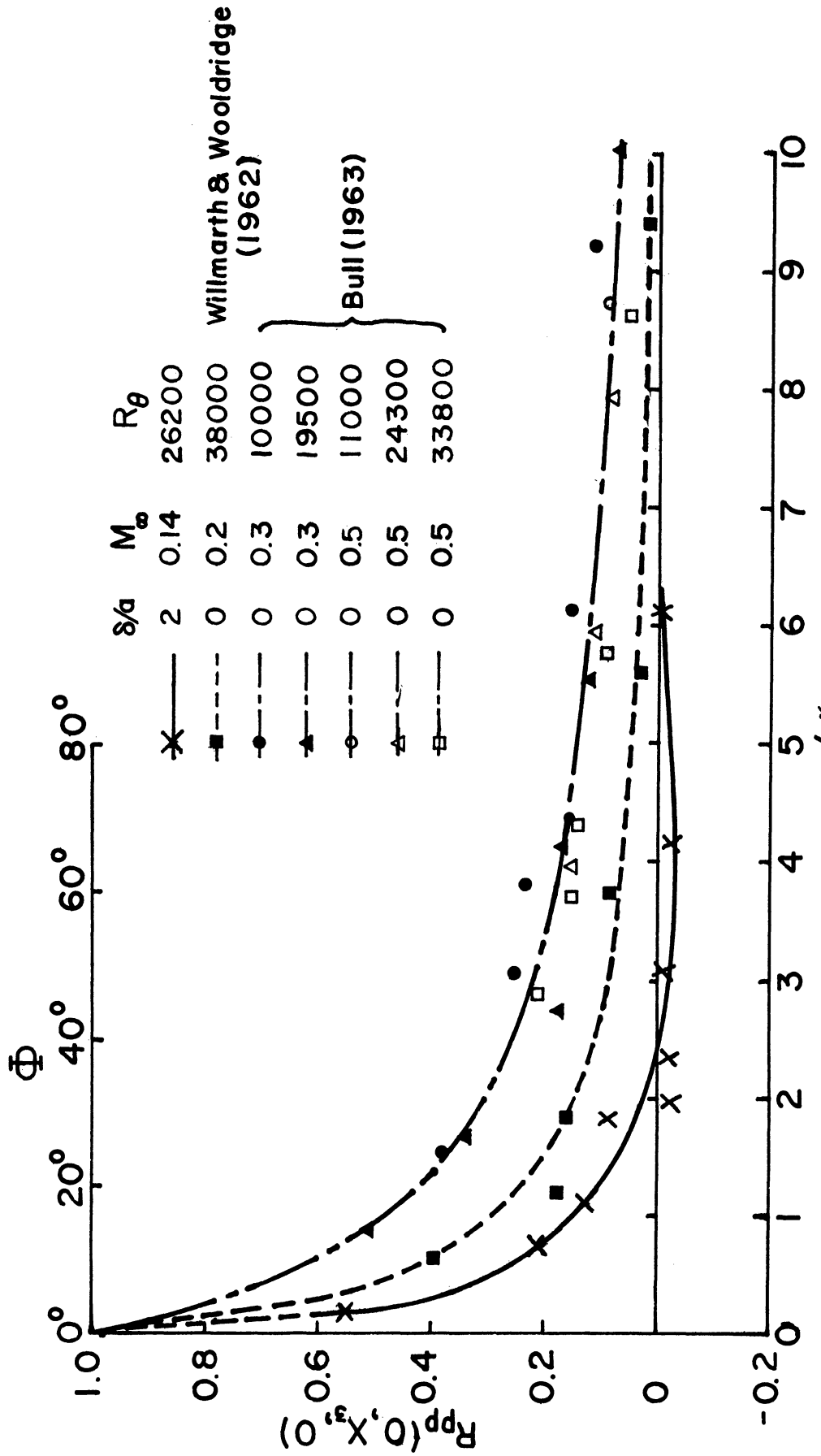

Figure 18. Transverse wall pressure correlation in a broad frequency band.

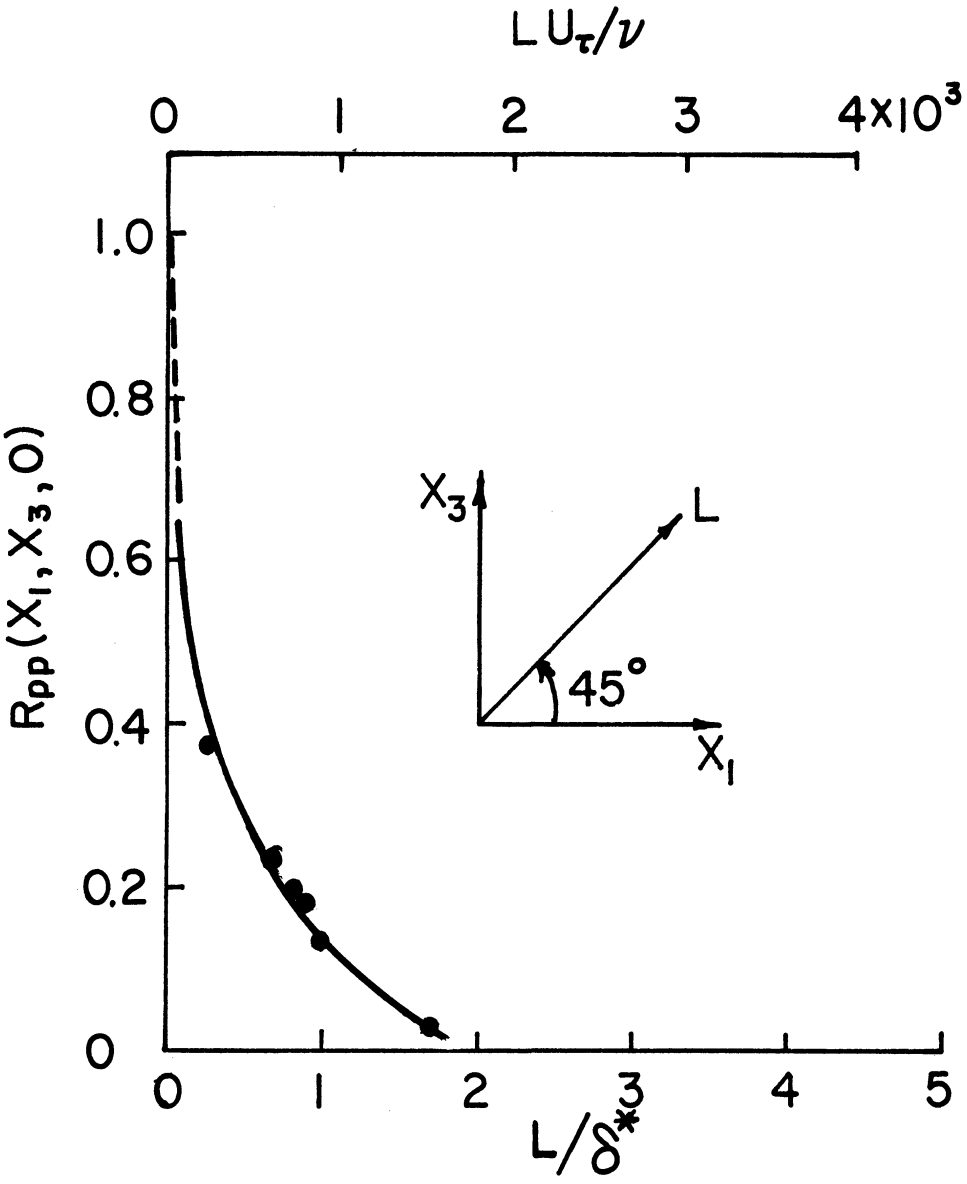

Figure 19. Spatial correlations of the wall pressure along a line at 45^o to the flow direction.

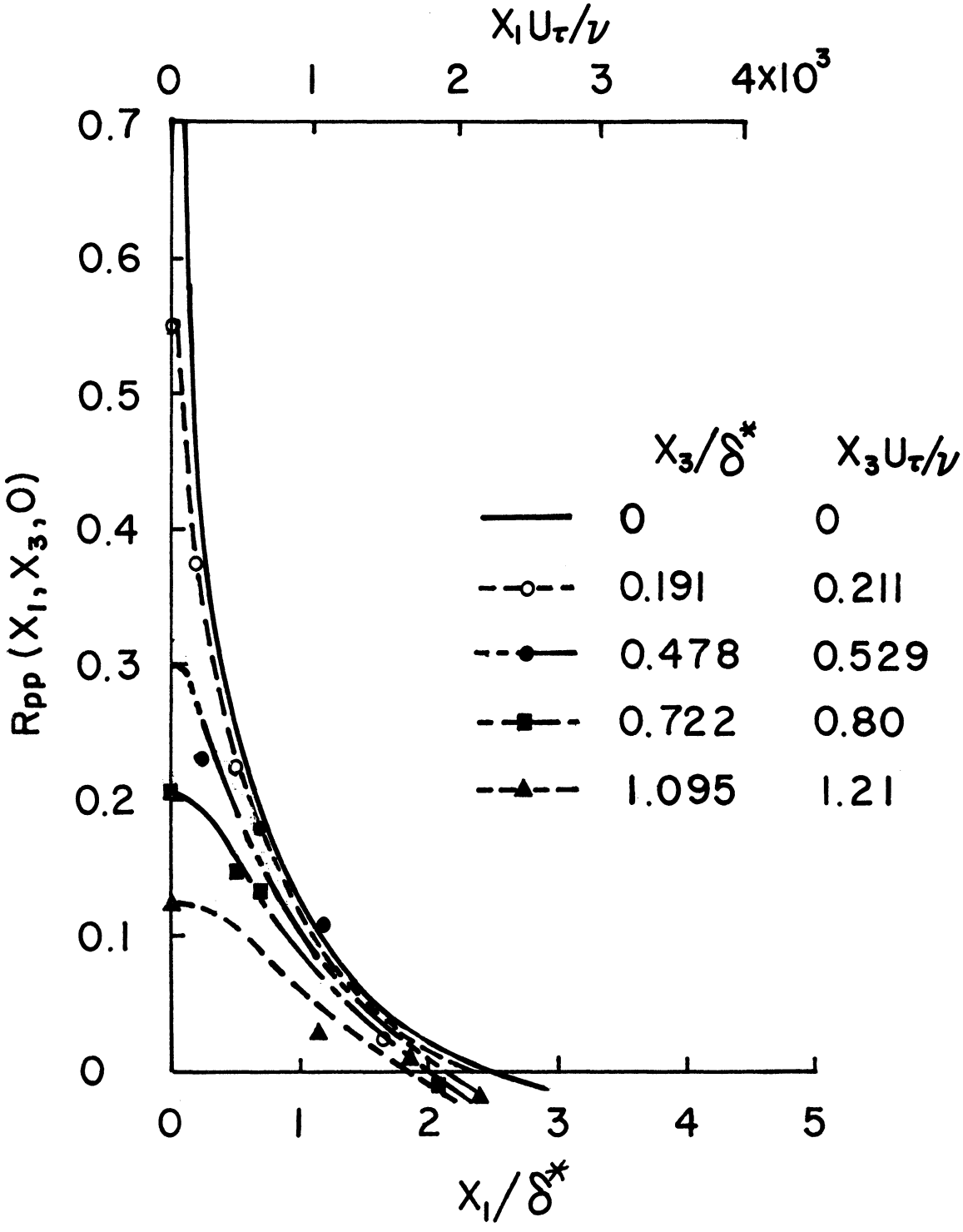

Figure 20. Spatial correlation of the wall pressure.

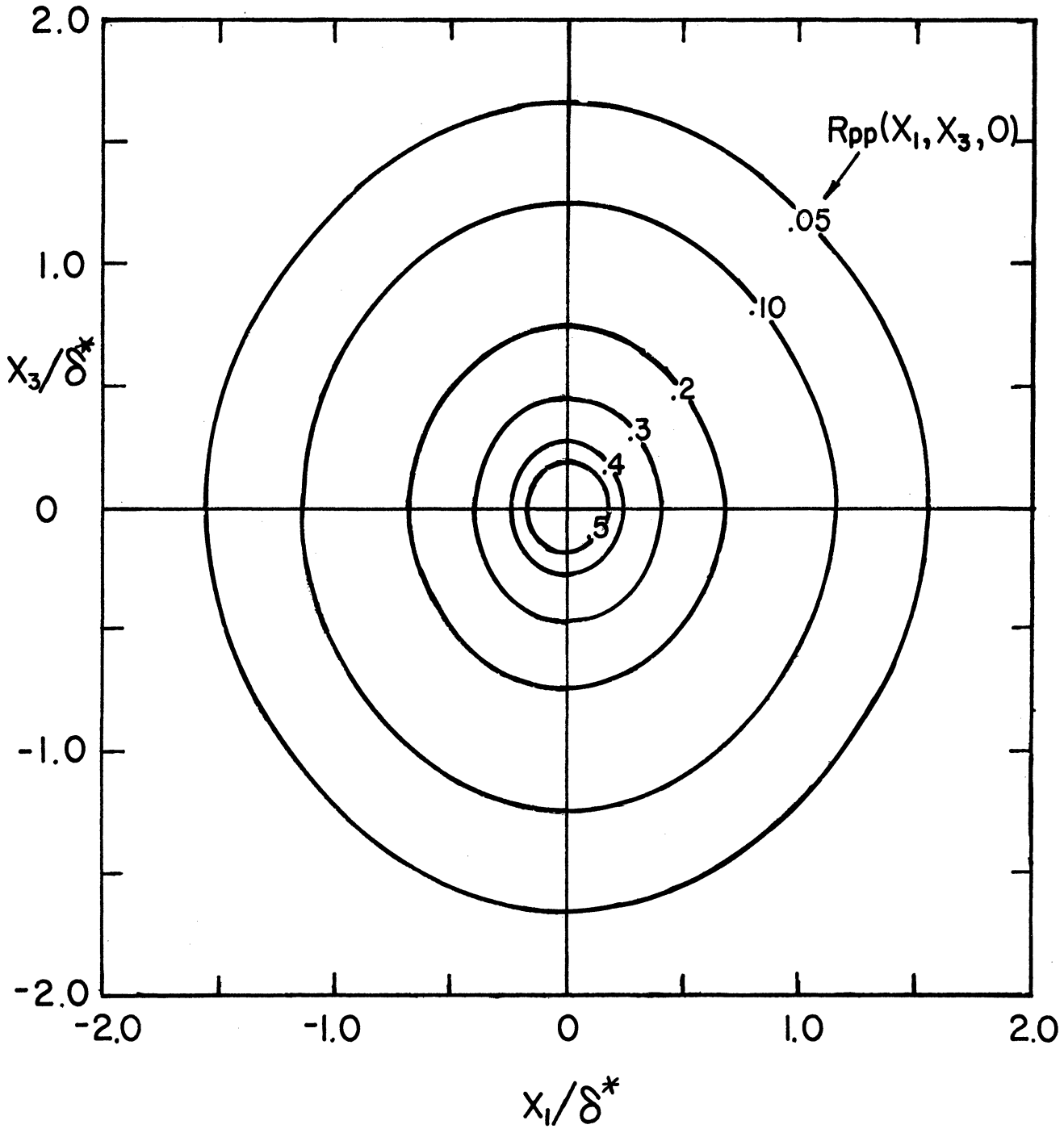

Figure 21. Contours of constant wall pressure correlation.

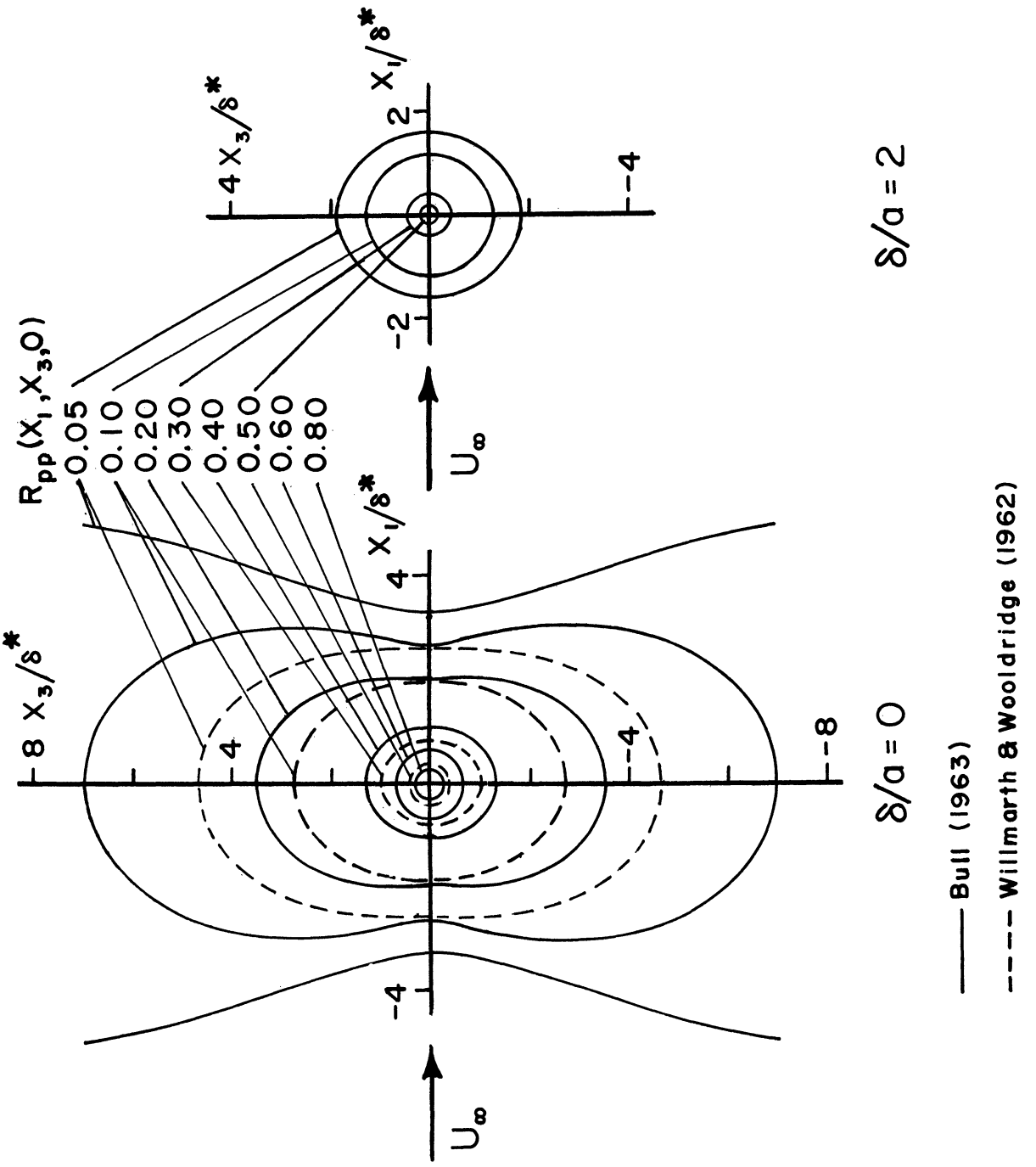

Figure 22. Effect of transverse curvature on wall pressure correlations.

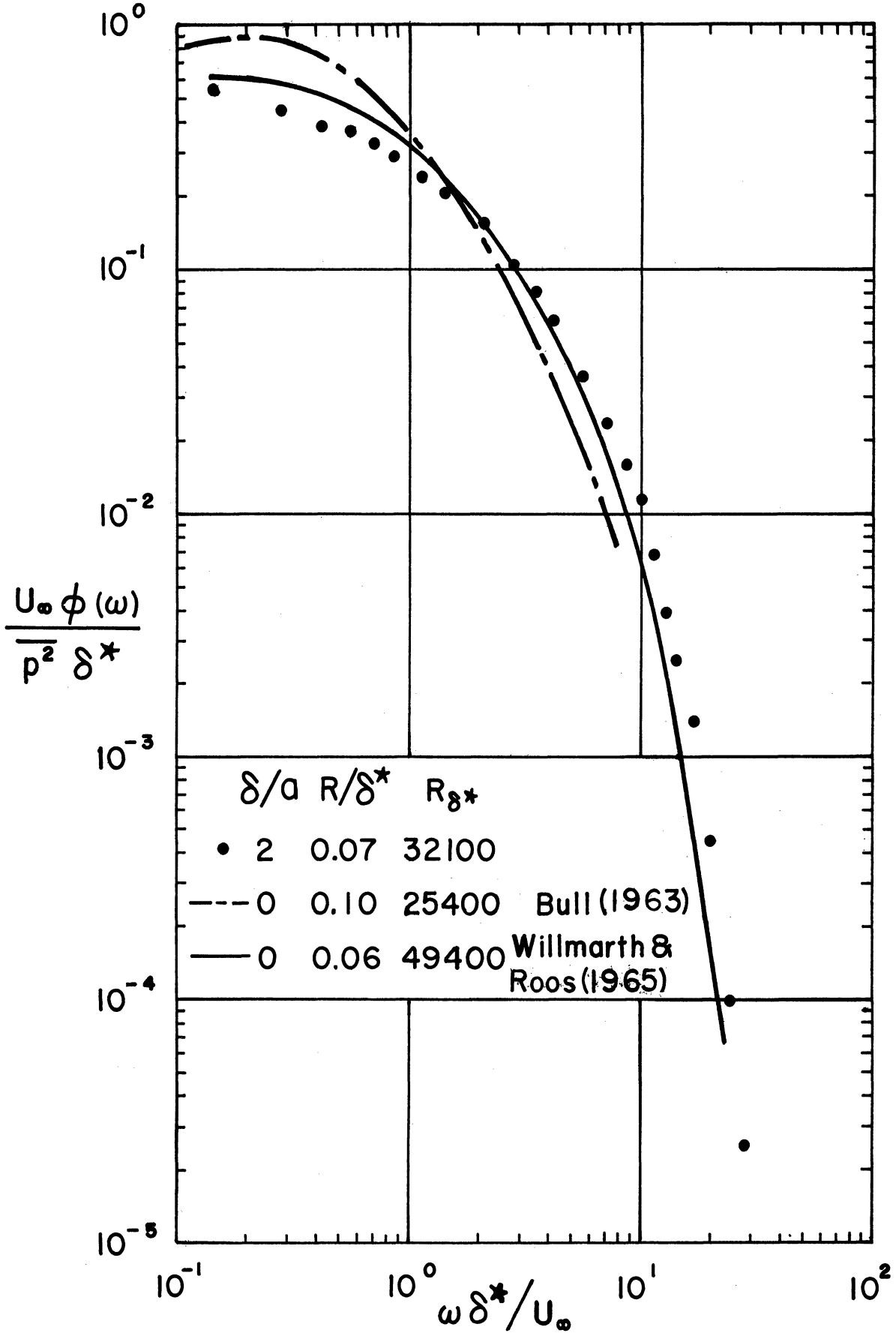

Figure 23. Measured wall pressure spectra.

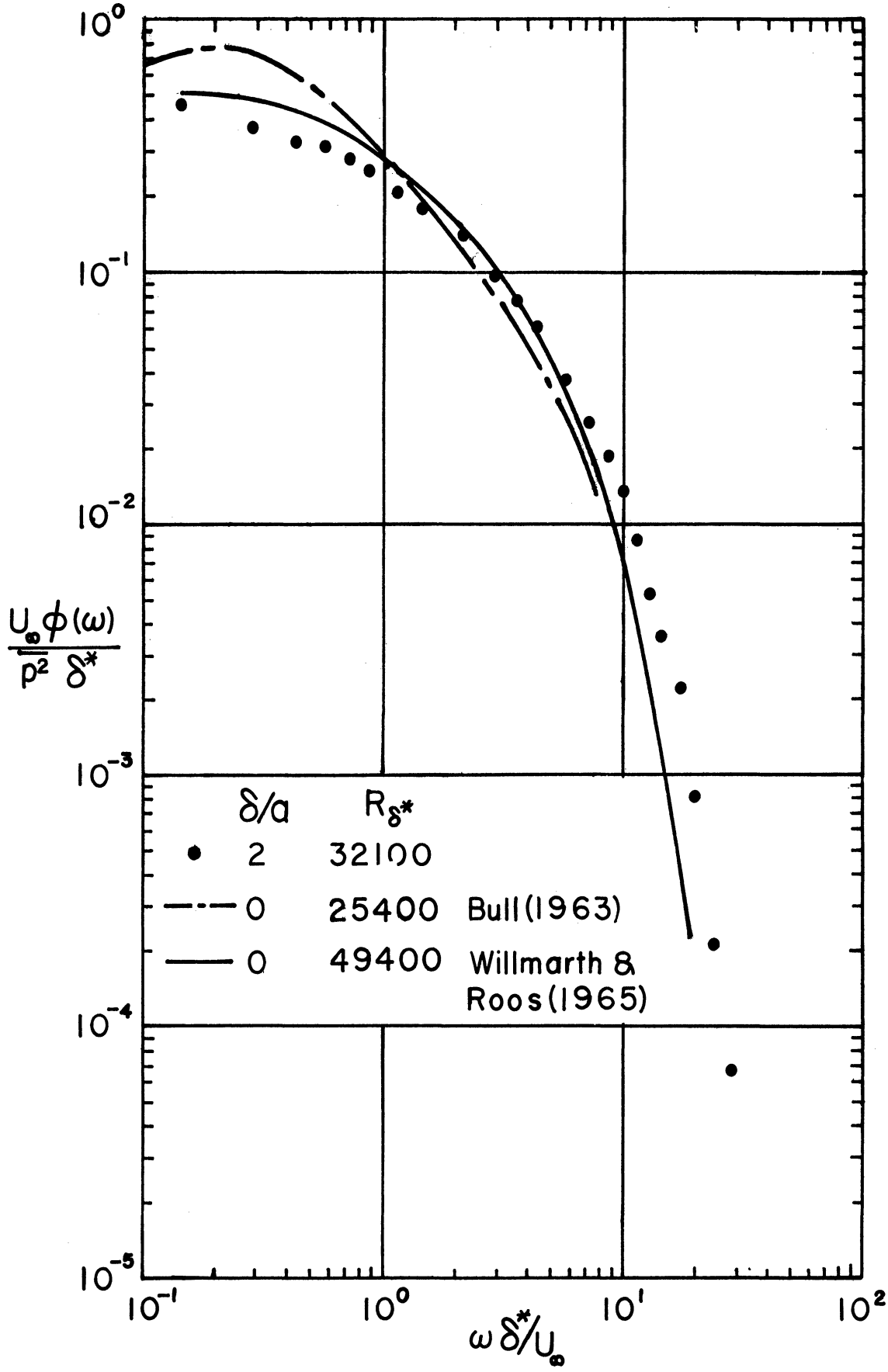

Figure 24. Corrected wall pressure spectra.

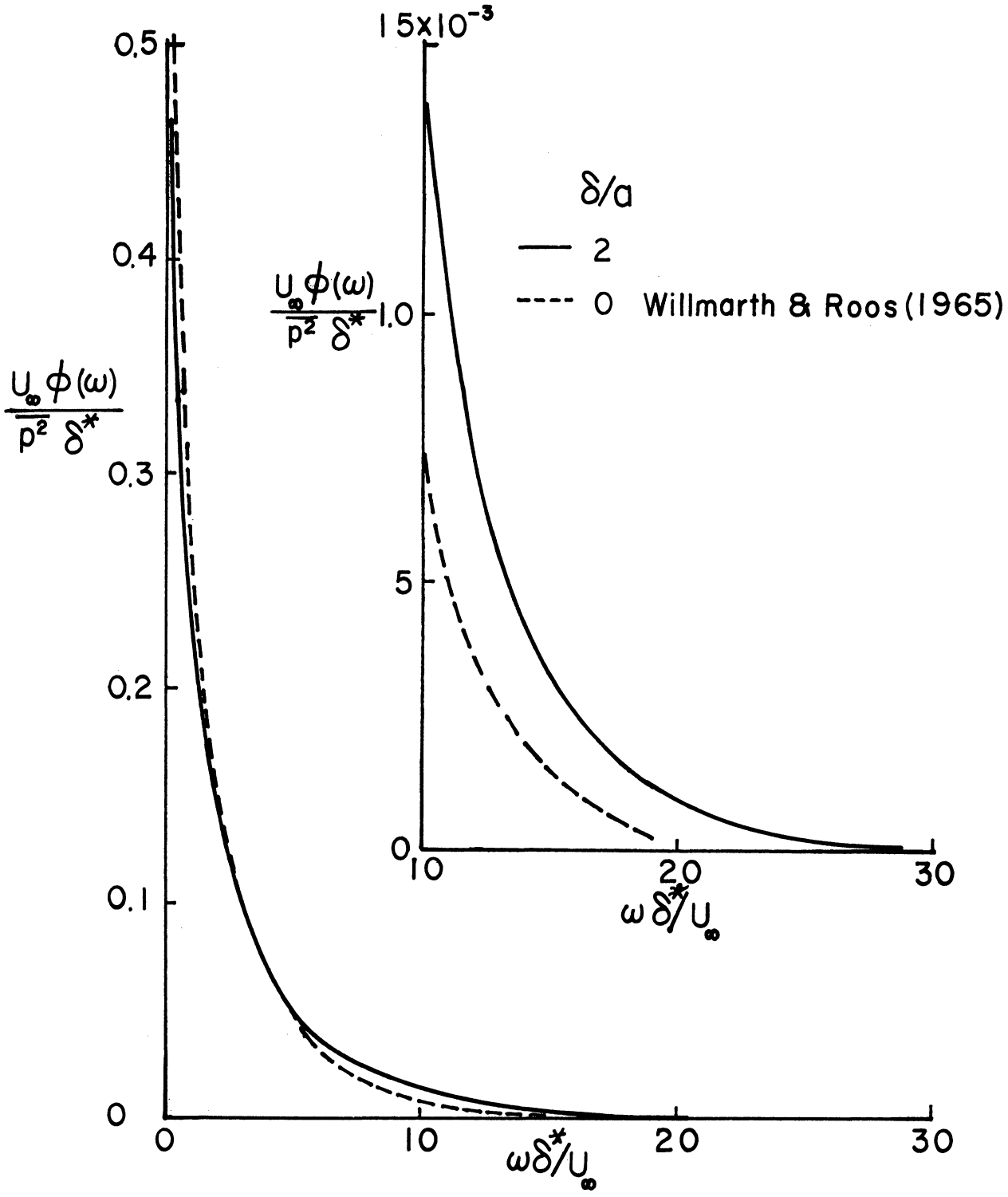

Figure 25. Corrected wall pressure spectra.

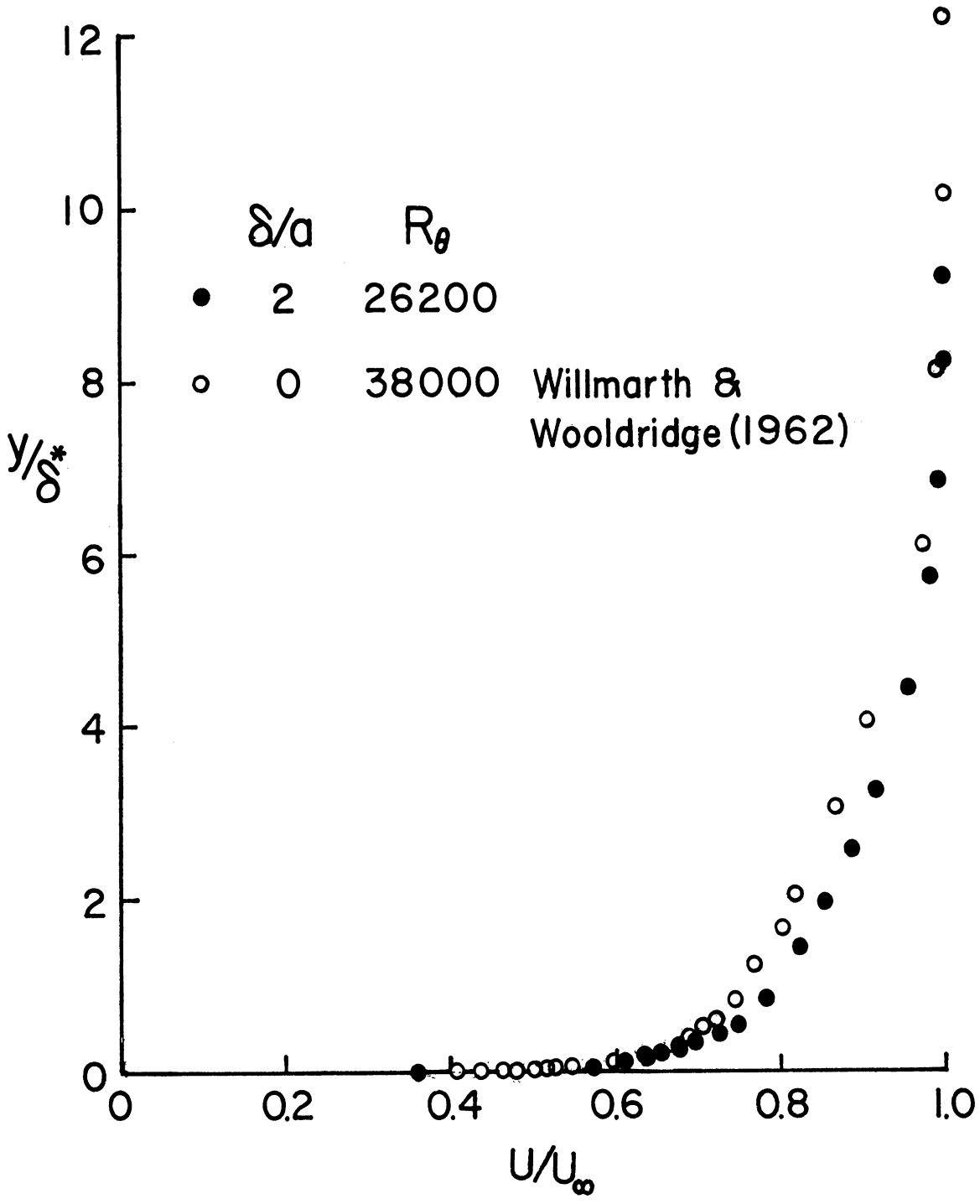

Figure 26. Comparison of the mean velocity profiles.

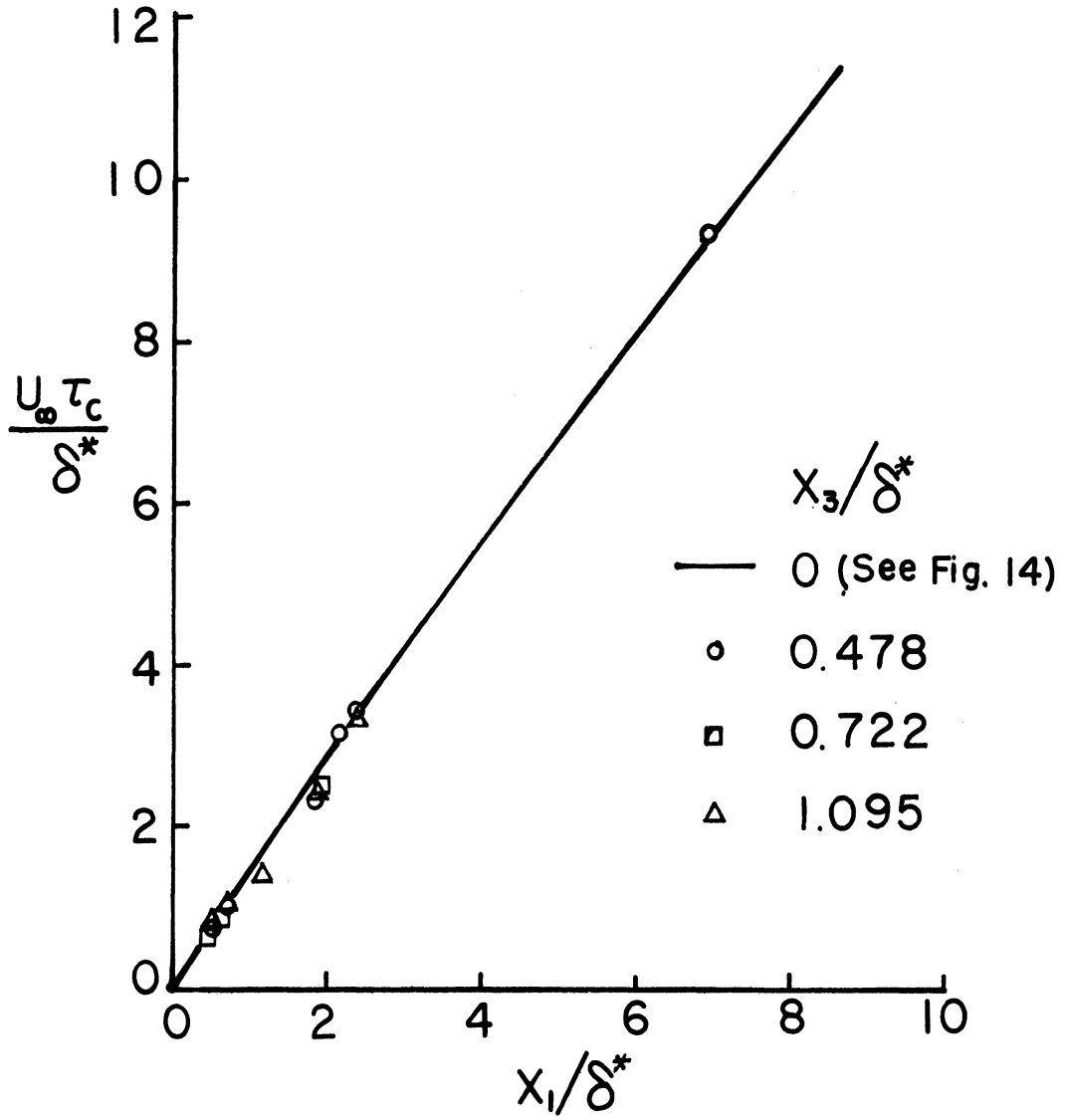

Figure 27. Time delay for R_{pp} maximum at constant x_1 for varied x_3.

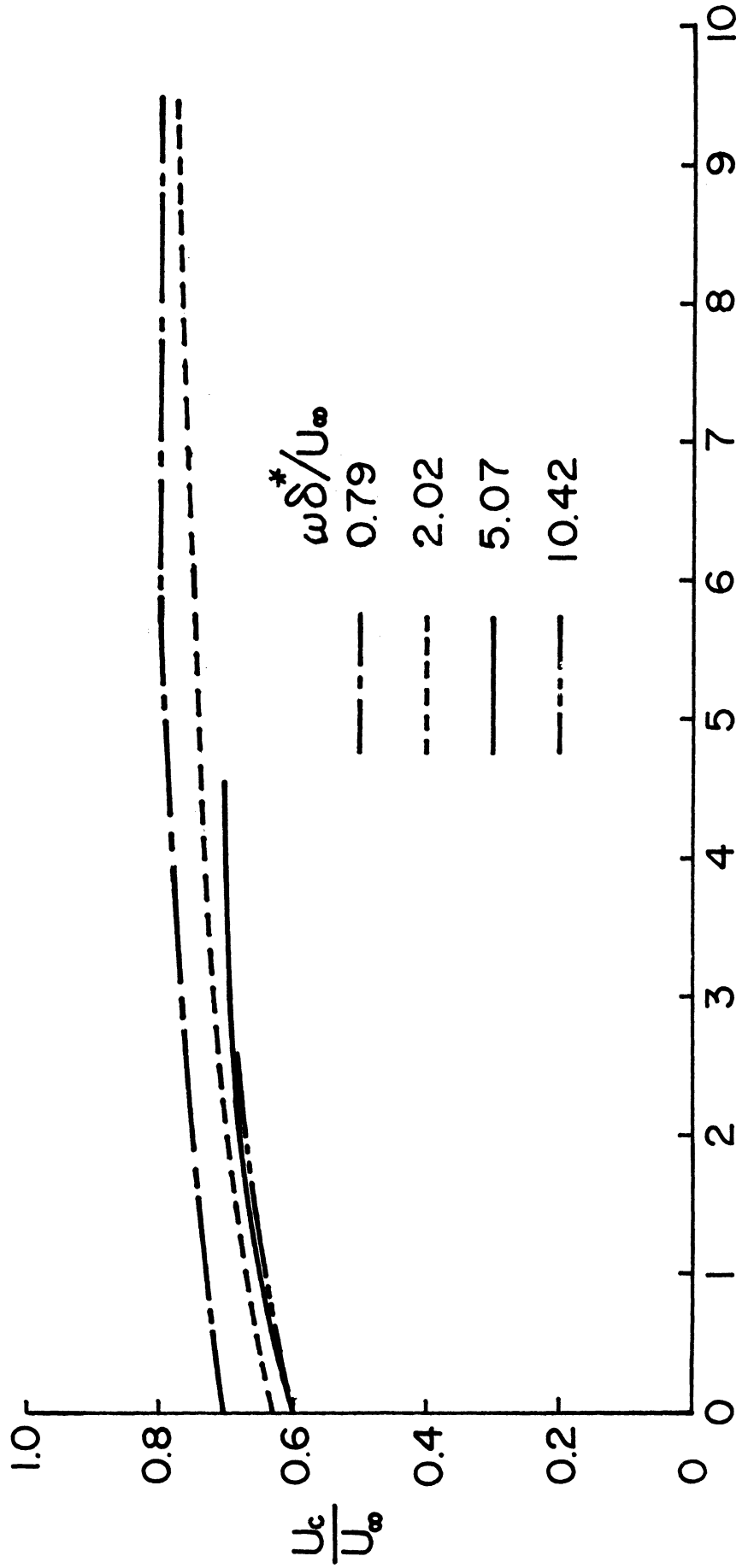

Figure 28. Local convection speed of pressure-producing turbulent eddies in various frequency bands.

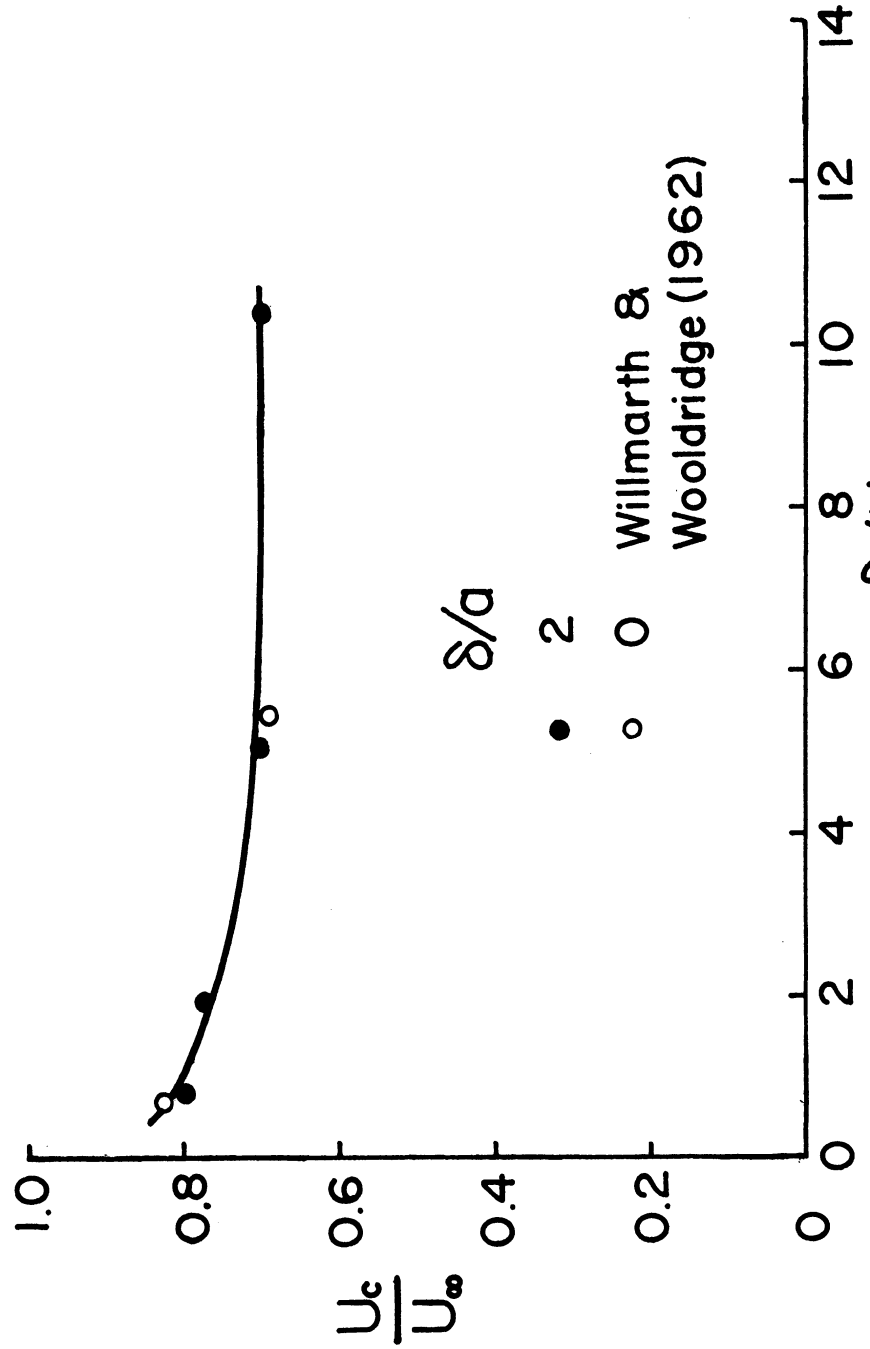

Figure 29. Asymptotic convection speed as a function of frequency.

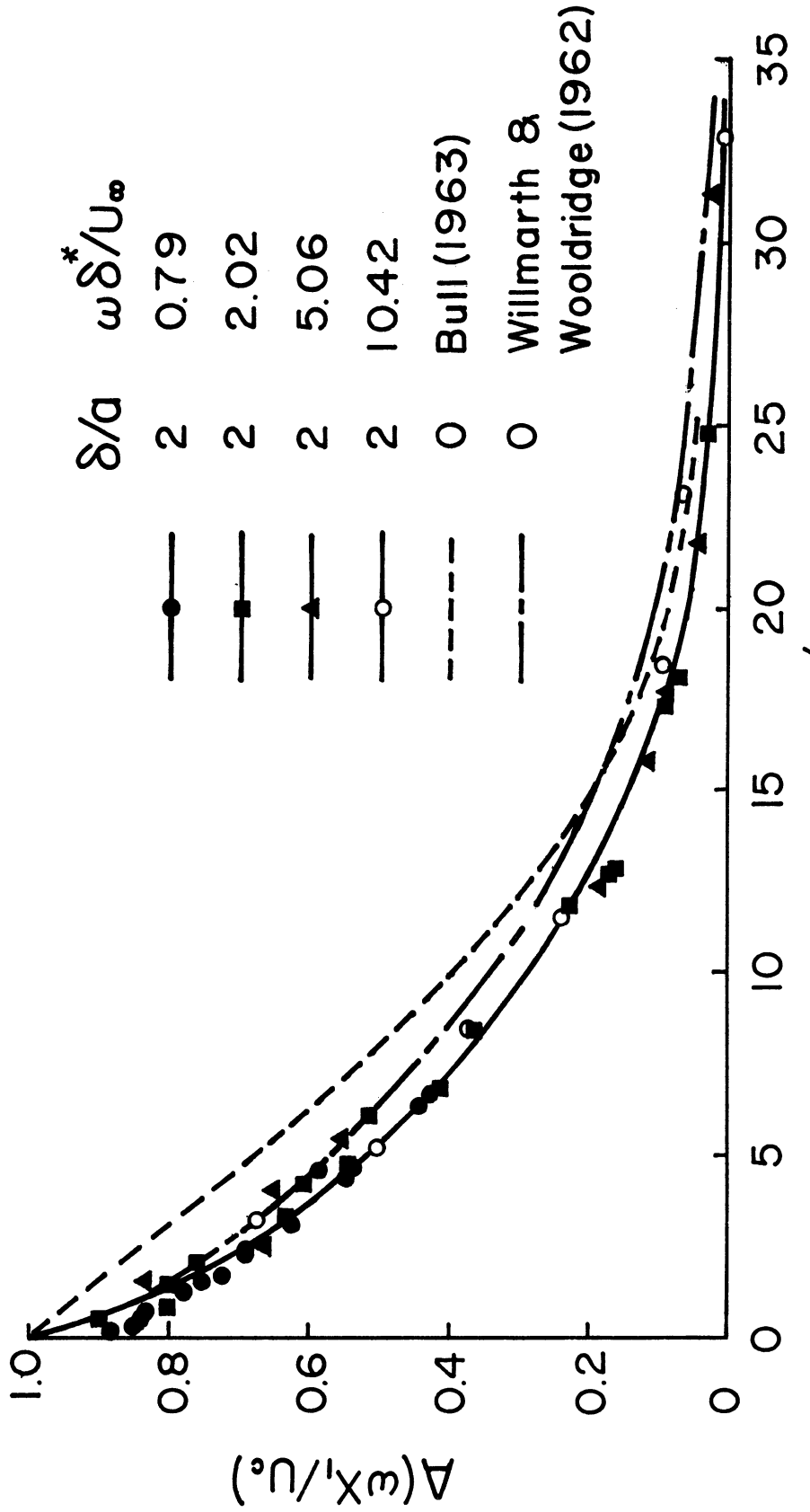

Figure 30. Amplitude of narrow-band longitudinal space-time correlation of the wall pressure.

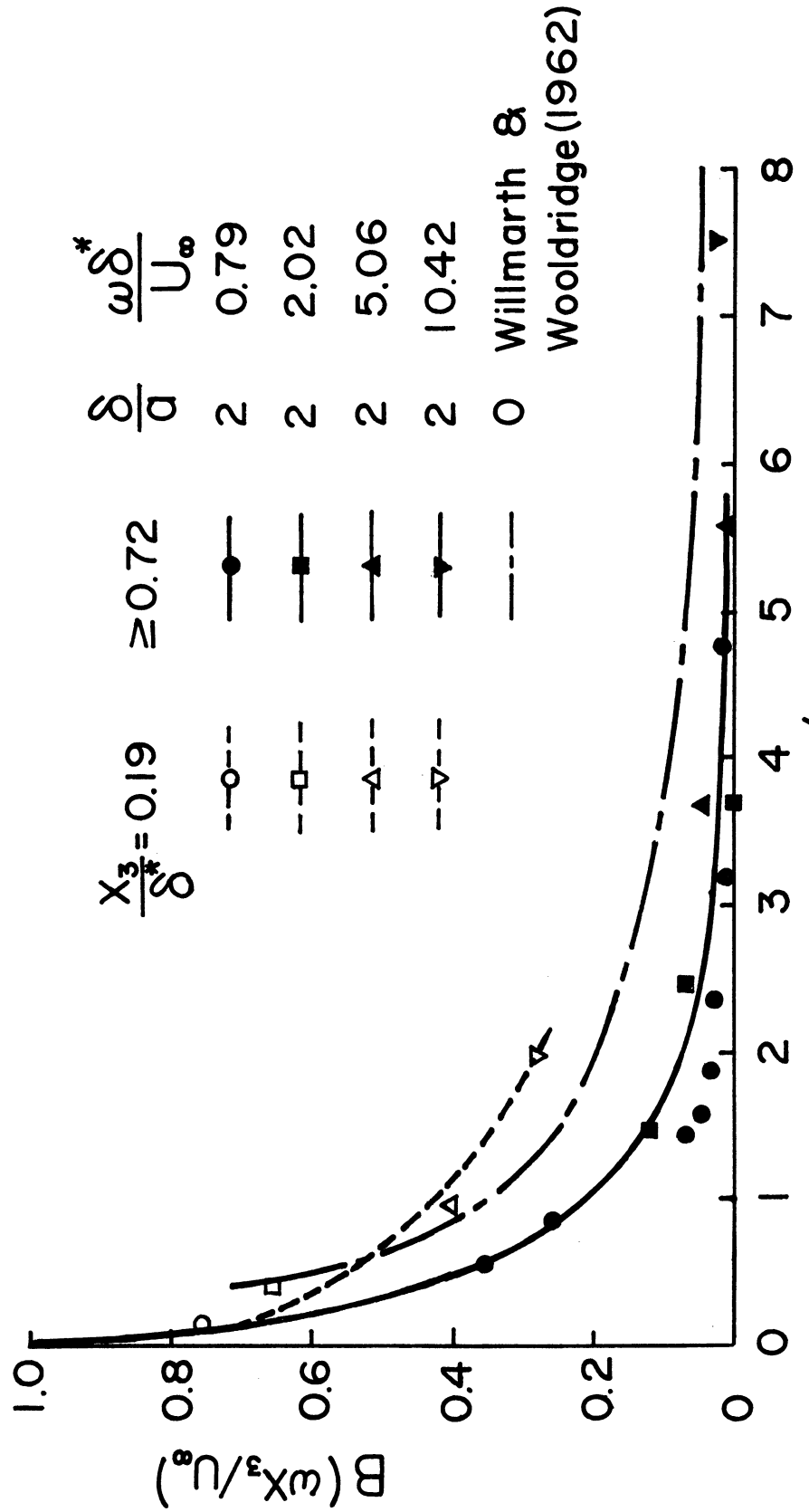

Figure 31. Amplitude of narrow-band transverse space-time correlation of the wall pressure.

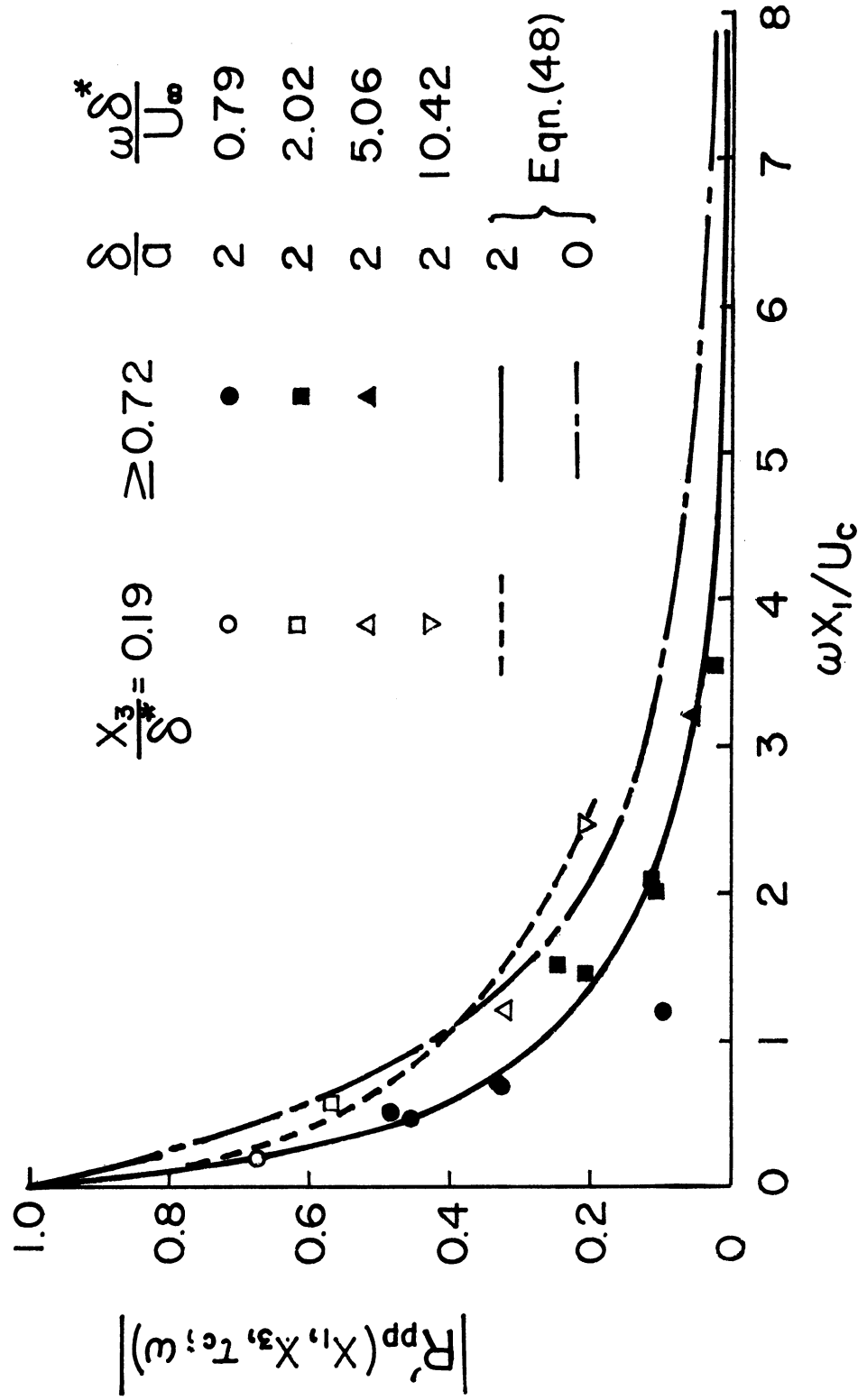

Figure 32. Amplitude of narrow-band space-time correlation of wall pressure along a line at 45^0 to the flow direction (Note $x_3 = x_1)_1$.

DISTRIBUTION LIST FOR UNCLASSIFIED
TECHNICAL REPORTS ISSUED UNDER
CONTRACT NO. N00014-67-A-0181-0015, TASK NO. 062-234

Technical Library
Building 131
Aberdeen Proving Ground, Maryland 21005

Defense Documentation Center (20)
Cameron Station
Alexandria, Virginia 22314

Technical Library
Naval Ship Research and
Development Center
Annapolis Division
Annapolis, Maryland 21402

Professor Bruce Johnson
Engineering Department
Naval Academy
Annapolis, Maryland 21402

Library
Naval Academy
Annapolis, Maryland 21402

Professor W. P. Graebel
Department of Engineering
Mechanics
The University of Michigan
College of Engineering
Ann Arbor, Michigan 48104

Professor W. R. Debler
Department of Engineering Mechanics
University of Mechanics
Ann Arbor, Michigan 48108

Dr. Francis Ogilvie
Department of Naval Architecture
and Marine Engineering
University of Michigan
Ann Arbor, Michigan 48108

Professor S. D. Sharma
Department of Naval Architecture
and Marine Engineering
University of Michigan
Ann Arbor, Michigan 48108

Professor W. W. Willmarth
Department of Aerospace Engineering
University of Michigan
Ann Arbor, Michigan 48108

Professor Finn C. Michelsen
Naval Architecture and Marine
Engineering
445 West Engineering Bldg.
University of Michigan
Ann Arbor, Michigan 48104

AFOSR (REM)
1400 Wilson Boulevard
Arlington, Virginia 22204

Dr. J. Menkes
Institute for Defense Analyses
400 Army-Navy Drive
Arlington, Virginia 22204

Professor S. Corrsin
Mechanics Department
The Johns Hopkins University
Baltimore, Maryland 20910

Professor O. M. Phillips
The Johns Hopkins University
Baltimore, Maryland 20910

Professor L. S. G. Kovasznay
The Johns Hopkins University
Baltimore, Maryland 20910

Librarian
Department of Naval Architecture
University of California
Berkeley, California 94720

Professor P. Lieber
Department of Mechanical Engineering
University of California
Institute of Engineering Research
Berkeley, California 94720

Professor M. Holt
Division of Aeronautical Sciences
University of California
Berkeley, California 94720

Professor J. V. Wehausen
Department of Naval Architecture
University of California
Berkeley, California 94720

Professor J. R. Paulling
Department of Naval Architecture
University of California
Berkeley, California 94720

Professor E. V. Laitone
Department of Mechanical Engineering
University of California
Berkeley, California 94720

School of Applied Mathematics
Indiana University
Bloomington, Indiana 47401

Commander
Boston Naval Shipyard
Boston, Massachusetts 02129

Director
Office of Naval Research
Branch Office
495 Summer Street
Boston, Massachusetts 02210

Professor M. S. Uberoi
Department of Aeronautical Engineering
University of Colorado
Boulder, Colorado 80303

Naval Applied Science Laboratory
Technical Library
Bldg. 1 Code 222
Flushing and Washington Avenues
Brooklyn, New York 11251

Professor J. J. Foody
Chairman, Engineering Department
State University of New York
Maritime College
Bronx, New York 10465

Dr. Irving C. Statler, Head
Applied Mechanics Department
Cornell Aeronautical Laboratory, Inc.
P. O. Box 235
Buffalo, New York 14221

Dr. Alfred Ritter
Assistant Head, Applied Mechanics Dept.
Cornell Aeronautical Laboratory, Inc.
Buffalo, New York 14221

Professor G. Birkhoff
Department of Mathematics
Harvard University
Cambridge, Massachusetts 02138

Commanding Officer
NROTC Naval Administrative Unit
Massachusetts Institute of Technology
Cambridge, Massachusetts 02139

Professor N. Newman
Department of Naval Architecture and
Marine Engineering
Massachusetts Institute of Technology
Cambridge, Massachusetts 02139

Professor A. H. Shapiro
Department of Mechanical Engineering
Massachusetts Institute of Technology
Cambridge, Massachusetts 02139

Professor C. C. Lin
Department of Mathematics
Massachusetts Institute of Technology
Cambridge, Massachusetts 02139

Professor E. W. Merrill
Department of Mathematics
Massachusetts Institute of Technology
Cambridge, Massachusetts 02139

Professor M. A. Abkowitz
Department of Naval Architecture
and Marine Engineering
Massachusetts Institute of Technology
Cambridge, Massachusetts 02139

Professor G. H. Carrier
Department of Engineering and
Applied Physics
Harvard University
Cambridge, Massachusetts 02139

Professor E. Mollo-Christensen
Room 54-1722
Massachusetts Institute of Technology
Cambridge, Massachusetts 02139

Professor A. T. Ippen
Department of Civil Engineering
Massachusetts Institute of Technology
Cambridge, Massachusetts 02139

Commander
Charleston Naval Shipyard
U. S. Naval Base
Charleston, South Carolina 29408

A. R. Kuhlthau, Director
Research Laboratories for the
Engineering Sciences
Thorton Hall, University of Virginia
Charlottesville, Virginia 22903

Director
Office of Naval Research
Branch Office
219 Dearborn Street
Chicago, Illinois 60604

Library
Naval Weapons Center
China Lake, California 93557

Library MS 60-3
NASA Lewis Research Center
21000 Brookpark Road
Cleveland, Ohio 44135

Professor J. M. Burgers
Institute of Fluid Dynamics and
Applied Mathematics
University of Maryland
College Park, Maryland 20742

Acquisition Director
NASA Scientific & Technical
Information
P. O. Box 33
College Park, Maryland 20740

Professor Pai
Institute for Fluid Dynamics
and Applied Mathematics
University of Maryland
College Park, Maryland 20740

Technical Library
Naval Weapons Laboratory
Dahlgren, Virginia 22448

Computation & Analyses Laboratory
Naval Weapons Laboratory
Dahlgren, Virginia 22448

Professor C. S. Wells
LTV Research Center
Dallas, Texas 75222

Dr. R. H. Kraichnan
Dublin, New Hampshire 03444

Commanding Officer
Army Research Office
Box CM, Duke Station
Durham, North Carolina 27706

Professor A. Charnes
The Technological Institute
Northwestern University
Evanston, Illinois 60201

Dr. Martim H. Bloom
Polytechnic Institute of Brooklyn
Graduate Center, Dept. of Aerospace
Engineering and Applied Mechanics
Farmingdale, New York 11735

Technical Documents Center
Building 315
U. S. Army Mobility Equipment
Research and Development Center
Fort Belvoir, Virginia 22060

Professor J. E. Cermak
College of Engineering
Colorado State University
Ft. Collins, Colorado 80521

Technical Library
Webb Institute of Naval Architecture
Glen Cove, Long Island, New York 11542

Professor E. V. Lewis
Webb Institute of Naval Architecture
Glen Cove, Long Island, New York 11542

Library MS 185
NASA, Langley Research Center
Langley Station
Hampton, Virginia 23365

Dr. B. N. Pridmore Brown
Northrop Corporation
NORAIR-Div.
Hawthorne, California 90250

Dr. J. P. Breslin
Stevens Institute of Technology
Davidson Laboratory
Hoboken, New Jersey 07030

Mr. D. Savitsky
Stevens Institute of Technology
Davidson Laboratory
Hoboken, New Jersey 07030

Mr. C. H. Henry
Stevens Institute of Technology
Davidson Laboratory
Hoboken, New Jersey 07030

Professor J. F. Kennedy, Director
Iowa Institute of Hydraulic Research
State University of Iowa
Iowa City, Iowa 52240

Professor L. Landweber
Iowa Institute of Hydraulic Research
State University of Iowa
Iowa City, Iowa 52240

Professor E. L. Resler
Graduate School of
Aeronautical Engineering
Cornell University
Ithaca, New York 14851

Professor John Miles
% I.G.P.P.
University of California, San Diego
La Jolla, California 92038

Director
Scripps Institution of Oceanography
University of California
La Jolla, California 92037

Dr. B. Sternlicht
Mechanical Technology Incorporated
968 Albany-Shaker Road
Latham, New York 12110

Mr. P. Eisenberg, President
Hydronautics
Pindell School Road
Howard County
Laurel, Maryland 20810 (2)

Professor A. Ellis
University of California, San Diego
Department of Aerospace & Mech. Engrg. Sci.
La Jolla, California 92037

Mr. Alfonso Alcedan L. Director
Laboratorio Nacional De Hydraulics
Antigui Cameno A. Ancon
Casilla Jostal 682
Lima, Peru

Commander
Long Beach Naval Shipyard
Long Beach, California 90802

Professor John Laufer
Department of Aerospace Engineering
University Park
Los Angeles, California 90007

Professor J. Ripkin
St. Anthony Falls Hydraulic Lab.
University of Minnesota
Minneapolis, Minnesota 55414

Professor J. M. Killen
St. Anthony Falls Hydraulic Lab.
University of Minnesota
Minneapolis, Minnesota 55414

Lorenz G. Straub Library
St. Anthony Falls Hydraulic Lab.
Mississippi River at 3rd Avenue SE.
Minneapolis, Minnesota 55414

Dr. E. Silberman
St. Anthony Falls Hydraulic Lab.
University of Minnesota
Minneapolis, Minnesota 55414

Superintendent
Naval Postgraduate School
Library Code 0212
Monterey, California 93940

Professor A. B. Metzner
University of Delaware
Newark, New Jersey 19711

Technical Library
USN Underwater Weapons &
Research & Engineering Station
Newport, Rhode Island 02840

Technical Library
Underwater Sound Laboratory
Fort Trumbull
New London, Connecticut 06321

Professor J. J. Stoker
Institute of Mathematical Sciences
New York University
251 Mercer Street
New York, New York 10003

Engineering Societies Library
345 East 47th Street
New York, New York 10017

Office of Naval Research
New York Area Office
207 W. 24th Street
New York, New York 10011

Commanding Officer
Office of Naval Research
Branch Office
Box 39
FPO New York, New York 09510 (25)

Professor H. Elrod
Department of Mechanical Engineering
Columbia University
New York, New York 10027

Society of Naval Architects and
Marine Engineering
74 Trinity Place
New York, New York 10006

Professor S. A. Piascek
Department of Engineering Mechanics
University of Notre Dame
Notre Dame, Indiana 46556

United States Atomic Energy Commission
Division of Technical Information
Extension
P. O. Box 62
Oak Ridge, Tennessee 37830

Miss O. M. Leach, Librarian
National Research Council
Aeronautical Library
Montreal Road
Ottawa 7, Canada

Technical Library
Naval Ship Research and
Development Center
Panaman City, Florida 32401

Library
Jet Propulsion Laboratory
California Institute of Technology
4800 Oak Grove Avenue
Pasadena, California 91109

Professor M. S. Plesset
Engineering Division
California Institute of Technology
Pasadena, California 91109

Professor H. Liepmann
Department of Aeronautics
California Institute of Technology
Pasadena, California 91109

Technical Library
Naval Undersea Warfare Center
3202 E. Foothill Boulevard
Pasadena, California 91107

Dr. J. W. Hoyt
Naval Undersea Warfare Center
3202 E. Foothill Boulevard
Pasadena, California 91107

Professor T. Y. Wu
Department of Engineering
California Institute of Technology
Pasadena, California 91109

Director
Office of Naval Research
Branch Office
1030 E. Green Street
Pasadena, California 91101

Professor A. Acosta
Department of Mechanical Engineering
California Institute of Technology
Pasadena, California 91109

Naval Ship Engineering Center
Philadelphia Division
Technical Library
Philadelphia, Pennsylvania 19112

Technical Library (Code 249B)
Philadelphia Naval Shipyard
Philadelphia, Pennsylvania 19112

Professor R. C. Mac Camy
Department of Mathematics
Carnegie Institute of Technology
Pittsburgh, Pennsylvania 15213

Dr. Paul Kaplan
Oceanics, Inc.
Plainview, Long Island, New York 11803

Technical Library
Naval Missile Center
Point Mugu, California 93441

Technical Library
Naval Civil Engineering Lab.
Port Hueneme, California 93041

Commander
Portsmouth Naval Shipyard
Portsmouth, New Hampshire 03801

Commander
Norfolk Naval Shipyard
Portsmouth, Virginia 23709

Professor F. E. Bisshopp
Division of Engineering
Brown University
Providence, Rhode Island 02912

Dr. L. L. Higgins
TRW Space Technology Labs, Inc.
One Space Park
Redondo Beach, California 90278

Redstone Scientific Information Center
Attn: Chief, Document Section
Army Missile Command
Redstone Arsenal, Alabama 35809

Dr. H. N. Abramson
Southwest Research Institute
8500 Culebra Road
San Antonio, Texas 78228

Editor
Applied Mechanics Review
Southwest Research Institute
8500 Culebra Road
San Antonio, Texas 78206

Librarian
Naval Command Control Communications
Laboratory Center
San Diego, California 92152

Library & Information Services
General Dynamics-Convair
P. O. Box 1128
San Diego, California 92112

Commander (Code 246P)
Pearl Harbor Naval Shipyard
Box 400
FPO San Francisco, California 96610

Technical Library (Code H245C-3)
Hunters Point Division
San Francisco Bay Naval Shipyard
San Francisco, California 94135

Office of Naval Research
San Francisco Area Office
1076 Mission Street
San Francisco, California 94103

Dr. A. May
Naval Ordnance Laboratory
White Oak
Silver Spring, Maryland 20910

Fenton Kennedy Document Library
The Johns Hopkins University
Applied Physics Laboratory
8621 Georgia Avenue
Silver Spring, Maryland 20910

Librarian
Naval Ordnance Laboratory
White Oak
Silver Spring, Maryland 20910

Dr. Bryne Perry
Department of Civil Engineering
Stanford University
Stanford, California 94305

Professor Milton Van Dyke
Department of Aeronautical Engineering
Stanford University
Stanford , California 94305

Professor E. Y. Hsu
Department of Civil Engineering
Stanford University
Stanford, California 94305

Dr. R. L. Street
Department of Civil Engineering
Stanford University
Stanford, California 94305

Professor S. Eskinazi
Department of Mechanical Engineering
Syracuse University
Syracuse, New York 13210

Professor R. Pfeffer
Florida State University
Geophysical Fluid Dynamics Institute
Tallahassee, Florida 32306

Professor J. Foa
Department of Aeronautical Engineering
Rennsselaer Polytechnic Institute
Troy, New York 12180

Professor R. C. Di Prima
Department of Mathematics
Rennsselaer Polytechnic Institute
Troy, New York 12180

Dr. M. Sevik
Ordnance Research Laboratory
Pennsylvania State University
University Park, Pennsylvania 16801

Professor J. Lumley
Ordnance Research Laboratory
Pennsylvania State University
University Park, Pennsylvania 16801

Dr. J. M. Robertson
Department of Theoretical and
Applied Mechanics
University of Illinois
Urbana, Illinois 61803

Shipyard Technical Library
Code 130L7 Building 746
San Francisco Bay Naval Shipyard
Vallejo, California 94592

Code L42
Naval Ship Research and
Development Center
Washington, D.C. 20007

Code 800
Naval Ship Research and
Development Center
Washington, D.C. 20007

Code 2027
U. S. Naval Research Laboratory
Washington, D.C. 20390 (6)

Code 438
Chief of Naval Research
Department of the Navy
Washington, D.C. 20360 (3)

Code 513
Naval Ship Research and
Development Center
Washington, D.C. 20007

Science & Technology Division
Library of Congress
Washington, D.C. 20540

ORD 913 (Library)
Naval Ordnance Systems Command
Washington, D.C. 20360

Code 6420
Naval Ship Engineering Center
Concept Design Division
Washington, D.C. 20360

Code 500
Naval Ship Research and
Development Center
Washington, D.C. 20007

Code 901
Naval Ship Research and
Development Center
Washington, D.C. 20007

Code 520
Naval Ship Research and
Development Center
Washington, D.C. 20007

Code 0341
Naval Ship Systems Command
Department of the Navy
Washington, D.C. 20360

Code 2052 (Technical Library)
Naval Ship Systems Command
Department of the Navy
Washington, D.C. 20360

Mr. J. L. Schuler (Code 03412)
Naval Ship Systems Command
Department of the Navy
Washington, D.C. 20360

Dr. J. H. Huth (Code 031)
Naval Ship Systems Command
Department of the Navy
Washington, D.C. 20360

Code 461
Chief of Naval Research
Department of the Navy
Washington, DC. 20360

Code 530
Naval Ship Research and
Development Center
Washington, D.C. 20360

Code 466
Chief of Naval Research
Department of the Navy
Washington, .D.C. 20360

Office of Research and Development
Maritime Administration
441 G. Street, NW.
Washington, D.C. 20235

Code 463
Chief of Naval Research
Department of the Navy
Washington, D.C. 20360

National Science Foundation
Engineering Division
1800 G. Street, NW.
Washington, D.C. 20550

Dr. G. Kulin
National Bureau of Standards
Washington, D.C. 20234

Department of the Army
Coastal Engineering Research Center
5201 Little Falls Road, NW.
Washington, D.C. 20011

Code 521
Naval Ship Research and
Development Center
Washington, D.C. 20007

Code 481
Chief of Naval Research
Department of the Navy
Washington, D.C. 20390

Code 421
Chief of Naval Research
Department of the Navy
Washington, D.C. 20360

Commander
Naval Ordnance Systems Command
Code ORD 035
Washington, D.C. 20360

Librarian Station 5-2
Coast Guard Headquarters
1300 E. Street, NW.
Washington, D.C. 20226

Division of Ship Design
Maritime Administration
441 G. Street, NW.
Washington, D.C. 20235

HQ USAF (AFRSTD)
Room 1D 377
The Pentagon
Washington, D.C. 20330

Commander
Naval Ship Systems Command
Code 6644C
Washington, D.C. 20360

Code 525
Naval Ship Research and
Development Center
Washington, D.C. 20007

Dr. A. Powell (Code 01)
Naval Ship Research and
Development Center
Washington, D.C. 20007

Director of Research Code RR
National Aeronautics & Space Admin.
600 Independence Avenue, SW.
Washington, D.C. 20546

Commander
Naval Ordnance Systems Command
Code 03
Washington, D.C. 20360

Code ORD 05411
Naval Ordnance Systems Command
Washington, D.C. 20360

AIR 5301
Naval Air Systems Command
Department of the Navy
Washington, D.C. 20360

AIR 604
Naval Air Systems Command
Department of the Navy
Washington, D.C. 20360

Dr. John Craven (PM 1100)
Deep Submergence Systems
Project
Department of the Navy
Washington, D.C. 20360

Code 522
Naval Ship Research and
Development Center
Washington, D.C. 20007

Commander
Naval Oceanographic Office
Washington, D.C. 20390

Chief of Research & Development
Office of Chief of Staff
Department of the Army
The Pentagon, Washington, D.C. 20310

Code 6342A
Naval Ship Systems Commmand
Department of the Navy
Washington, D.C. 20360

Code 468
Chief of Naval Research
Department of the Navy
Washington, D.C. 20360

Director
U. S. Naval Research Laboratory
Code 6170
Washington, D.C. 20390

Code 473
Chief of Naval Research
Department of the Navy
Washington, D.C. 20360

Code 6100
Naval Ship Engineering Center
Department of the Navy
Washington, D.C. 20360

Mr. Ralph Lacey (Code 6114)
Naval Ship Engineering Center
Department of the Navy
Washington, D.C. 20360

Dr. A. S. Iberall, President
General Technical Services, Inc.
451 Penn Street
Yeadon, Pennsylvania 19050

Dr. H. Cohen
IBM Research Center
P. O. Box 218
Yorktown Heights, New York 10598

Unclassified

Security Classification

DOCUMENT CONTROL DATA - R & D

(Security classification of title, body of abstract and indexing annotation must be entered when the overall report is classified)

1. ORIGINATING ACTIVITY (Corporate author)	2a. REPORT SECURITY CLASSIFICATION
The University of Michigan Department of Aerospace Engineering Ann Arbor, Michigan	Unclassified
	2b. GROUP Not applicable

3. REPORT TITLE

Wall Pressure Fluctuations Beneath an Axially Symmetric Turbulent Boundary Layer on a Cylinder

4. DESCRIPTIVE NOTES (Type of report and inclusive dates)

Technical Report

5. AUTHOR(S) (First name, middle initial, last name)

Chi-Sheng Yang and William W. Willmarth

6. REPORT DATE	7a. TOTAL NO. OF PAGES	7b. NO. OF REFS
August 1969	89	26

8a. CONTRACT OR GRANT NO.	9a. ORIGINATOR'S REPORT NUMBER(S)
N 00014-67-A-0181-0015 b. PROJECT NO. c. d.	02149-1-T 9b. OTHER REPORT NO(S) (Any other numbers that may be assigned this report)

10. DISTRIBUTION STATEMENT

This document has been approved for public release and sale; its distribution is unlimited.

11. SUPPLEMENTARY NOTES	12. SPONSORING MILITARY ACTIVITY
	Office of Naval Research

13. ABSTRACT

Measurements of the turbulent pressure field on the outer surface of a 3 inch diameter cylinder were made at a point 24 feet downstream of the origin of the turbulent boundary layer. The root-mean square wall pressure was 2.42 times the wall shear stress. The normalized power spectrum at high frequencies ($\omega\delta^*/U_\infty > 10$) contained twice the energy density of the spectrum beneath a plane boundary layer. The convection speed was the same as that in a plane boundary layer but the eddy size was smaller by a factor of two. The smaller eddy size and unchanged convection speed account for the greater energy in the spectrum at high frequencies.

DD FORM 1 NOV 65 1473

Unclassified

Security Classification

14. KEY WORDS	LINK A		LINK B		LINK C	
	ROLE	WT	ROLE	WT	ROLE	WT
Turbulent Pressure Turbulent boundary layer Wall pressure fluctuations						